11-2005

Modification of Precipitation by Coastal Orography in Storms Crossing Northern California

Curtis N. James
Embry-Riddle Aeronautical University, james61c@erau.edu

Robert A. Houze Jr.
University of Washington - Seattle Campus

Scholarly Commons Citation

Modification of Precipitation by Coastal Orography in Storms Crossing Northern California

CURTIS N. JAMES

Department of Meteorology, Embry-Riddle Aeronautical University, Prescott, Arizona

ROBERT A. HOUZE JR.

Department of Atmospheric Sciences, University of Washington, Seattle, Washington

ABSTRACT

This study compiles and interprets three-dimensional Weather Surveillance Radar-1988 Doppler (WSR-88D) data during a 2.5-yr period and examines the typical orographic effects on precipitation mainly associated with winter storms passing over coastal northern California.

The three-dimensional mean reflectivity patterns show echo structure that was generally stratiform from over the ocean to inland over the mountains. The flow above the 1-km level was strong enough to be unblocked by the terrain, and the mean echo pattern over land had certain characteristics normally associated with an unblocked cross-barrier flow, both on the broad scale of the windward slopes of the coastal mountains and on the scale of individual peaks of the terrain on the windward side. Upward-sloping echo contours on the scale of the overall region of coastal mountains indicated broadscale upslope orographic enhancement. On a smaller scale, the mean stratiform echo pattern over the mountains contained a strong embedded core of maximum reflectivity over the first major peak of terrain encountered by the unblocked flow and a secondary echo core over the second major rise of the coastal mountain terrain.

Offshore, upstream of the coastal mountains, the reflectivity pattern showed a region of enhanced mainly stratiform echo within ~100 km of the coast, with an embedded echo core, similar to those over the inland mountain peaks, along its leading edge. It is suggested that the offshore enhancement is caused by intensified frontogenesis in the offshore coastal zone and/or by the onshore directed low-level flow rising over a thin layer of cool, stable air dammed against the coastal mountains.

The orographically enhanced precipitation offshore and over the coastal mountains was present to some degree in all the landfalling storms. However, the degree to which each feature was present varied. All the features were more pronounced when the 500–700-hPa flow was strong, the midlevel humidity was high, and the low-level cross-barrier wind component was strong. When the low-level stability was greater, the offshore enhancement of precipitation was proportionately increased, and the general broadscale enhancement inland was reduced.

1. Introduction

Coastal northern California is an ideal laboratory for observing stable to weakly unstable orographic precipitation. Deep convection is rare along the West Coast, and heavy precipitation is usually associated with landfalling baroclinic systems that direct strong, moist low-level flow against the terrain from the Pacific Ocean (e.g., Nagle and Serebreny 1962; Elliott and Hovind 1964; Hobbs et al. 1975, 1980; Houze et al. 1976; Braun et al. 1997; Doyle 1997; Colle et al. 1999, 2002; Yu and Smull 2000; Neiman et al. 2004; Ralph et al. 2004). The terrain in the region contains quasi-two-dimensional mountain ridges that are analogous to traditional idealized model studies of flow over terrain (e.g., Queney 1948). The ridges are oriented from north-northwest to south-southeast and are approximately orthogonal to the prevailing low-level flow during heavy-precipitation events (Fig. 1). The South Fork Mountain and the King Range ridges will be prominent in the subsequent discussions of this paper.

Corresponding author address: Prof. C. N. James, Dept. of Meteorology, Embry-Riddle Aeronautical University, 3700 Willow Creek Road, Prescott, AZ 86301–3720.
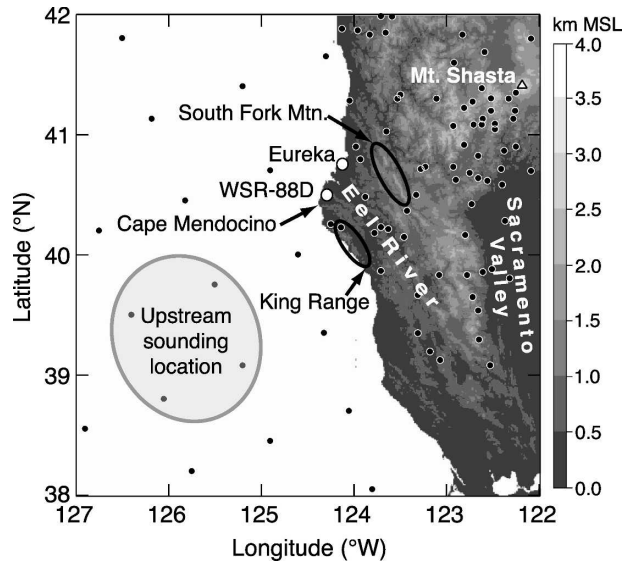E-mail: Curtis.James@erau.edu

FIG. 1. Digital terrain map of coastal northern California with terrain elevation shaded. The locations of important geographic features and the Eureka WSR-88D are labeled. Black-filled circles over land represent automated rain gauge stations; black dots over ocean depict the locations of Eta Model grid points. The four points enclosed by the ellipse were horizontally averaged to produce a synthetic sounding representative of the upstream flow.

When strong, moist, low-level wind interacts with the California coastal orography, heavy rainfall accumulation (up to 250 mm in a day) can occur. The rain may combine with rapid snowmelt and produce extreme flooding of local rivers and streams. During one flood in December 1964, the Eel River (Fig. 1) rose approximately 25 m above flood stage and reached a peak discharge rate of 21 300 $m^3 s^{-1}$ (Sommerfield et al. 2002). These extreme events can occur when the low-level jet (LLJ) required by hydrostatic and semigeostrophic balance ahead of a front conveys moisture and heat into the region of the mountains for a prolonged period of time, sometimes for several days (Ralph et al. 2004, 2005). Floods occur in the European Alps for much the same reason, as the low-level moist jet ahead of a front impinges on the barrier (Buzzi et al. 1998; Doswell et al. 1998; Rotunno and Ferretti 2001).

Browning (1986) emphasized the strong poleward sensible and latent heat flux in the LLJ to the east of an approaching cyclone by calling it a "warm conveyor belt." LLJs approaching the California coastline originate in the northern fringes of the Tropics and are correspondingly quite moist. Ralph et al. (2004) referred to the narrow belt of moisture flux within a warm conveyor belt as an "atmospheric river." When fronts approach the northern California coast, this narrow zone of moist flow is nearly always southwesterly, oriented

quasi-perpendicular to the two-dimensional ridges of the coastal mountains of northern California and thus in an optimal orientation for orographic modification of the precipitation associated with the passing baroclinic system.

The modification of the precipitation that occurs as the LLJ impinges on a mountain range is a multiscale process. The flow pattern in the baroclinic system is modified on the mesoscale, depending on the stratification of the temperature, moisture, and wind stratification of the impinging flow. Over the Alps, Houze et al. (2001, hereafter HJM) found that the basic pattern of precipitation enhancement depended on whether the upstream flow was blocked or unblocked. In the blocked cases, the enhancement began upstream of the barrier (as suggested, e.g., by Grossman and Durran 1984). In the unblocked cases, the enhancement occurred almost entirely over the lower slopes of the barrier with little activity upstream. Major Alpine floods occur primarily with the unblocked cases, in which the near-surface boundary layer air rises directly over the barrier, with little tendency to turn parallel to the barrier or flow around individual peaks. The unblocked cases are marked by rapid growth and fallout of precipitation over the lower windward slopes and especially over the first steep rise of the terrain (Buzzi et al. 1998; Doswell et al. 1998; HJM; Yuter and Houze 2003). In the combined case where lower-level flow is blocked and an upper layer is unblocked, it is also evident from the Mesoscale Alpine Program (MAP) that orographic precipitation enhancement can occur both upstream from and over a mountain barrier [the intensive observation period 8 (IOP8) case studied by Medina and Houze (2003, 2005) and Medina et al. (2005)]. In this paper, we suggest an analogous behavior occurs over coastal northern California, where the flow above 1 km is generally strong and largely unblocked but may have a lower layer of blocked flow also affecting the precipitation processes.

Small-scale processes also participate in orographic precipitation enhancement. Smith (1979) pointed out the likely importance of convective-scale cellularity for enhancing orographic precipitation particle growth by coalescence or riming. Elliott and Hovind (1964) suggested that precipitation associated with fronts passing over California indeed manifested embedded small convection cells, which they thought enhanced the total rainfall. Also examining California precipitation, White et al. (2003) suggested that small convective cells might enhance the rainout. They also suggested, on the microphysical scale, that the coalescence of liquid drops in the cloud layer below the 0°C level (sometimes referred

to as "warm rain") is an important microphysical mechanism producing precipitation fallout in storms passing over the coastal mountains of California. White et al. (2003) also showed, as will be shown in this paper, that major precipitation systems accounting for most of the rain in the northern California coastal region extend well above the 0°C level and exhibit a pronounced bright band, signaling that the ice phase is also important. Browning et al. (1975) suggested that both liquid-water coalescence and ice-phase processes contribute to high precipitation efficiencies in orographic precipitation. Yuter and Houze (2003) found that small cells embedded in orographic precipitation in baroclinic systems over the European Alps were important in enhancing the growth of precipitation particles both above and below the 0°C level. The rates of coalescence below and riming above the 0°C level were comparable within small-scale embedded updrafts. Medina and Houze (2005) have found that strong turbulent overturning in the shear layer separating a lower layer of retarded or blocked flow from an upper layer of unblocked flow may enhance the growth and fallout of precipitation particles on the windward slopes. Larger, deep convective cells can overwhelmingly dominate the precipitation over the windward slope if the flow over a mountain barrier is sufficiently unstable (e.g., Caracena et al. 1979); however, the northern California region in winter is not a favored location for deep convection, and the weak instability leads primarily to embedded shallow convection in a basically stratiform cloud layer.

In this study, we seek insight into the multiscale physical processes involved in orographic precipitation enhancement over the coastal mountains of northern California and how the nature of the enhancement varies with the strength, stability, and layering of the upstream flow. Achieving this objective will help determine whether processes occurring over this mountainous region are similar to or different from processes over the Alps and other major mountain ranges. We use the Weather Surveillance Radar-1988 Doppler (WSR-88D) operational radar data collected over a two-and-a-half-year period at Eureka, California (Fig. 1). This radar covers precipitation both over the ocean and as it crosses the windward slopes of the mountain barrier. This is not a study of rain measurement by radar. Rather, we aim to understand how the coastal mountains affect the physical processes of precipitation growth and fallout. To accomplish this aim, we compile time-mean three-dimensional patterns of radar reflectivity and radial velocity. By examining simultaneously the detailed mean spatial structure of both the reflectivity and radial velocity fields, we deduce aspects of the interplay of microphysics (indicated grossly by reflec-

tivity) and air motions (indicated by radial velocity). By further relating the radar reflectivity and velocity fields to the details of the topography of the terrain, we further infer how the orography modifies the microphysics and dynamics.

In section 2 of this paper, we describe the data and methods used in this study. Section 3 presents the large-scale setting of major rain events over the northern California coastal region. Section 4 describes the overall average three-dimensional radar echo climatology. Section 5 explains how we stratify the dataset into "epochs" defined by combinations of environmental variables. Section 6 discusses the variability of the radar echo climatology with respect to midlevel flow. Section 7 analyzes the orographic precipitation processes with respect to the wind velocity and stability of the low-level flow impinging on the mountains. Section 8 integrates all the results.

2. Data and methods

The basic dataset for this study is a two-and-a-half-year archive of major precipitation events from the Eureka, California, WSR-88D. This coastal radar, located near Cape Mendocino, has a relatively unimpeded view of precipitation over the mountains to its east and over the ocean to its west. This location (Fig. 1) allows sampling of precipitation systems as they approach the coast, make landfall, and move over the mountains. Terrain clutter and shadowing are less of a problem for the Eureka WSR-88D than other West Coast WSR-88D sites (Westrick et al. 1999). Archived level II data of reflectivity and radial velocity (Crum and Alberty 1993) were obtained for most of the heavy-precipitation days during 1 October 1995–31 March 1998, a period that included the California Landfalling Jets Experiment (CALJET; Ralph et al. 1999).

A major precipitation event was defined as a day on which at least 25% of the 73 automated rain gauges in the region bounded by 39°N, 42°N, 122°W, and the California coastline recorded 25 mm (1 in.) or more of precipitation. The black-filled circles in Fig. 1 show the locations of the gauges. Radar archives were available for 61 of the 67 heavy-precipitation days identified (Table 1). The basic unit of radar data was the three-dimensional volume scanned by the WSR-88D elevation angle sequence. To reduce autocorrelation and minimize data storage requirements, we reduced the time resolution of the radar data by using only the data volumes obtained at 1-h time intervals.

Since the radar processor's clutter suppression algorithm was insufficient to remove all terrain contamination, we developed a digital terrain mask. The terrain

TABLE 1. Heavy-rain days identified during 1 Oct 1995–31 Mar 1998 when WSR-88D archives were available.

1995	1996	1997	1998
11, 12, 14, 15 Dec	15, 16, 18, 27 Jan	1 Jan	2, 3, 11, 12, 14, 16, 18, 25, 26 Jan
	4, 17, 18, 19, 20 Feb	16 Mar	1, 2, 3, 5, 6, 7, 14, 16, 19, 21 Feb
	4 Mar	18 Apr	12, 21, 22, 23 Mar
	21 May	3 Jun	
	17, 18, 19 Nov	8 Oct	
	4, 7, 8, 9, 10, 26, 29, 30, 31 Dec	15, 16, 26, 29 Nov	
		7, 14 Dec	

mask used an equivalent-earth-radius ray-propagation model to approximate the altitude of the radar's lowest tilt (0.5°) at each radar gate (Doviak and Zrnic 1993, 14–23). The equivalent earth radius corresponding to the strongest vertical refractivity gradient of all 61 heavy-precipitation days was used to give a liberal estimate of the amount of beam refraction. Then, a terrain elevation dataset with 30-s spatial resolution was used to determine whether any terrain intersected the bottom of the radar beam within a horizontal latitude–longitude element of dimensions $1' \times 1'$. If the main lobe of the radar (width 0.94°) was intersected by terrain, then that range bin and all bins at farther range in that radial were removed. To reduce sidelobe contamination, if terrain was located within 0.5° of the bottom of the main lobe, then the corresponding radar bin was deleted. This technique removed virtually all terrain clutter and shadowing from the dataset and allowed all remaining radar reflectivity bins over terrain to be interpreted as precipitation rather than clutter contamination.

To remove noise, radial velocity data were removed if their corresponding reflectivity values were deleted or below a threshold of -10.0 dBZ. The radial velocity data were then dealiased using a University of Washington algorithm similar in construction to the WSR-88D algorithm (Eilts and Smith 1990). A small fraction of the volumes that were not successfully dealiased by the algorithm were rejected, leaving a total of 1176 for analysis. The volumes were bilinearly interpolated to a three-dimensional Cartesian grid with 2-km horizontal spacing and 0.5-km vertical spacing using the National Center for Atmospheric Research's (NCAR) SPRINT software (Mohr and Vaughan 1979) and finally converted to Unidata's Network Common Data Format (NetCDF) for analysis using MountainZebra (James et al. 2000), which is a version of NCAR's Zebra software (Corbet et al. 1994) in which the detailed terrain field is included. The interpolation grid, superposed with a vertical cross section of the most commonly used WSR-88D volume coverage pattern (VCP 21), is shown in Fig. 2.

Mean reflectivity and radial velocity were computed using the interpolated radar volumes. For reflectivity averaging, a missing value indicates absence of precipitation. Therefore, the reflectivity factor (mm^6 m^{-3}) at the corresponding grid point was set to zero. Missing radial velocity information, on the other hand, merely indicates the absence of scatterers. Therefore, the mean reflectivity factor $\overline{Z}$ and radial velocity $\overline{V}$ at each grid point were computed as

$$\overline{Z} = \frac{\sum_{i=1}^{N} Z_i}{N} \tag{1}$$

and

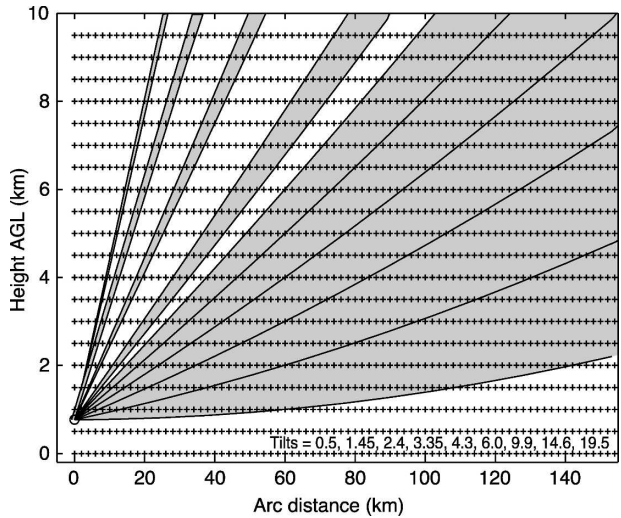$$\overline{V} = \frac{\sum_{i=1}^{n} V_i}{n}, \tag{2}$$

FIG. 2. Height vs range representation of the Eureka WSR-88D tilt sequence looking east from the radar site (indicated by the open circle at 767-m altitude and 0-km range). Each radar tilt is shaded, and interpolation grid points are indicated by "+." (Adapted from James et al. 2000.)

where N is the total number of volumes (=1176), and n ($\leq N$) is the number of volumes with nonmissing radial velocity values. From (1), it is evident that $\overline{Z}$ maxima indicate regions where the precipitation was either more frequent, more reflective, or both. Higher reflectivity is generally correlated with heavier rainfall. To reduce unwanted noise and radar artifacts, inverse range-squared horizontal smoothing was applied at each interpolation grid point within a 16-km horizontal radius of influence for all horizontal maps (6-km horizontal radius for vertical cross sections).

To investigate the sensitivity of rainfall to the upstream flow and stability, superposed epoch analyses (e.g., Reed and Recker 1971; HJM), or "composites," were constructed by dividing the radar volumes into subsets or *epochs* defined by some specific wind or thermodynamic condition. Then, the mean and standard deviation were computed at each grid point in the subset of volumes. The statistical significance of these subset means were indicated by two-sided Student's t difference-of-means tests that were performed at each grid point using an a priori confidence level of 95% (Spiegel 1972). As in HJM, the sample sizes in this study and the low autocorrelation between successive radar scans both appear to be adequate for difference-of-means tests (e.g., Wilks 1995).

The superposed epoch analyses led to conclusions about the sensitivity of the precipitation in the vicinity of Eureka to dynamic and thermodynamic variables of the large-scale flow offshore. We estimate these upstream variables using analyses and 6-h forecasts from a 90 km × 90 km × 50-hPa resolution National Centers for Environmental Prediction (NCEP) Eta Model grid. The model data at the four upstream model grid points bounded by the ellipse in Fig. 1 were horizontally averaged to produce smooth vertical soundings at 6-h intervals. If no model grid was available within 3 h of a radar-volume time, the volume was not used for those calculations that required sounding information. Model grids were available for 1116 of the radar volumes. The 700–500-hPa layer in the synthetic soundings was used to represent "midlevel" characteristics of the flow. The 900–800-hPa layer (~1–2 km MSL) in the synthetic soundings, corresponding to the LLJ altitude and the strongest correlation with precipitation (Neiman et al. 2002), was used to estimate the static stability, wind speed, wind direction, and dewpoint temperature upwind. The static stability was represented by the moist Brunt–Väisälä frequency (Durran and Klemp 1982) and was computed using finite differences.

Figure 3 summarizes the static stability estimates in the 900–800-hPa layer of onshore flow, as computed from the Eta Model output. The squared moist Brunt–
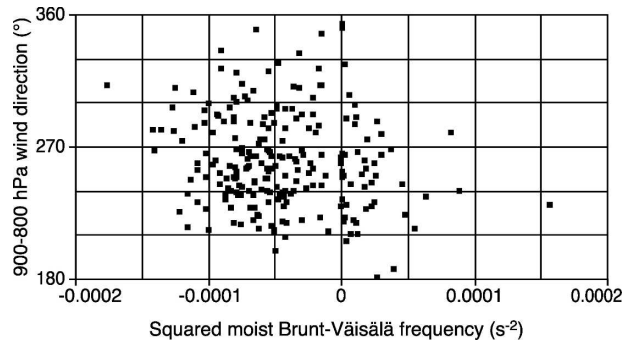

Fig. 3. The interdependence of squared moist Brunt–Väisälä frequency and wind direction in the 900–800-hPa layer over virtually all of the Eta-derived upstream soundings. Negative Brunt–Väisälä frequencies denote conditional instability in the 900–800-hPa layer.

Väisälä frequency was small in magnitude (i.e., less than 10^{-4} s^{-2}), indicating that deviation from moist neutrality was minimal, with some days being slightly moist-unstable and others slightly moist-stable. Furthermore, the 900–800-hPa stability was generally uncorrelated with wind direction, although northwest flows were seldom absolutely stable.

3. Large-scale flow and stability

Figures 4a and 4b show the mean large-scale synoptic conditions indicated by 12-hourly NCEP global model reanalysis output at 2.5° × 2.5° resolution for the major rain events (Kalnay et al. 1996). This map shows that on average the 1000- and 500-hPa flows were generally southwesterly, perpendicular to the mountain ranges of coastal northern California, consistent with Ralph et al. (2004) and other studies mentioned earlier. A baroclinic trough was located offshore with the maximum of large-scale upward motion located over the northern California coast. Figure 4 also depicts the mean synoptic maps for two subsets of cases. For reasons discussed in section 6, we focus on cases for which the 900–800-hPa flow was west-southwesterly, which produces the greatest orographic effect on the precipitation.

The west-southwesterly events are subdivided into days in which the thermodynamic stratification of the 900–800-hPa layer was slightly unstable or neutral versus absolutely stable. The large-scale mean synoptic patterns for the unstable/neutral cases (Figs. 4c,d) and stable cases (Figs. 4e,f) were qualitatively very similar, except that the stable events exhibited slightly weaker southwesterly gradient wind. The midlevel height patterns (Figs. 4d,f) were also very similar, with comparable 700-hPa upward motion between unstable and unstable events. The 700-hPa vertical motion patterns
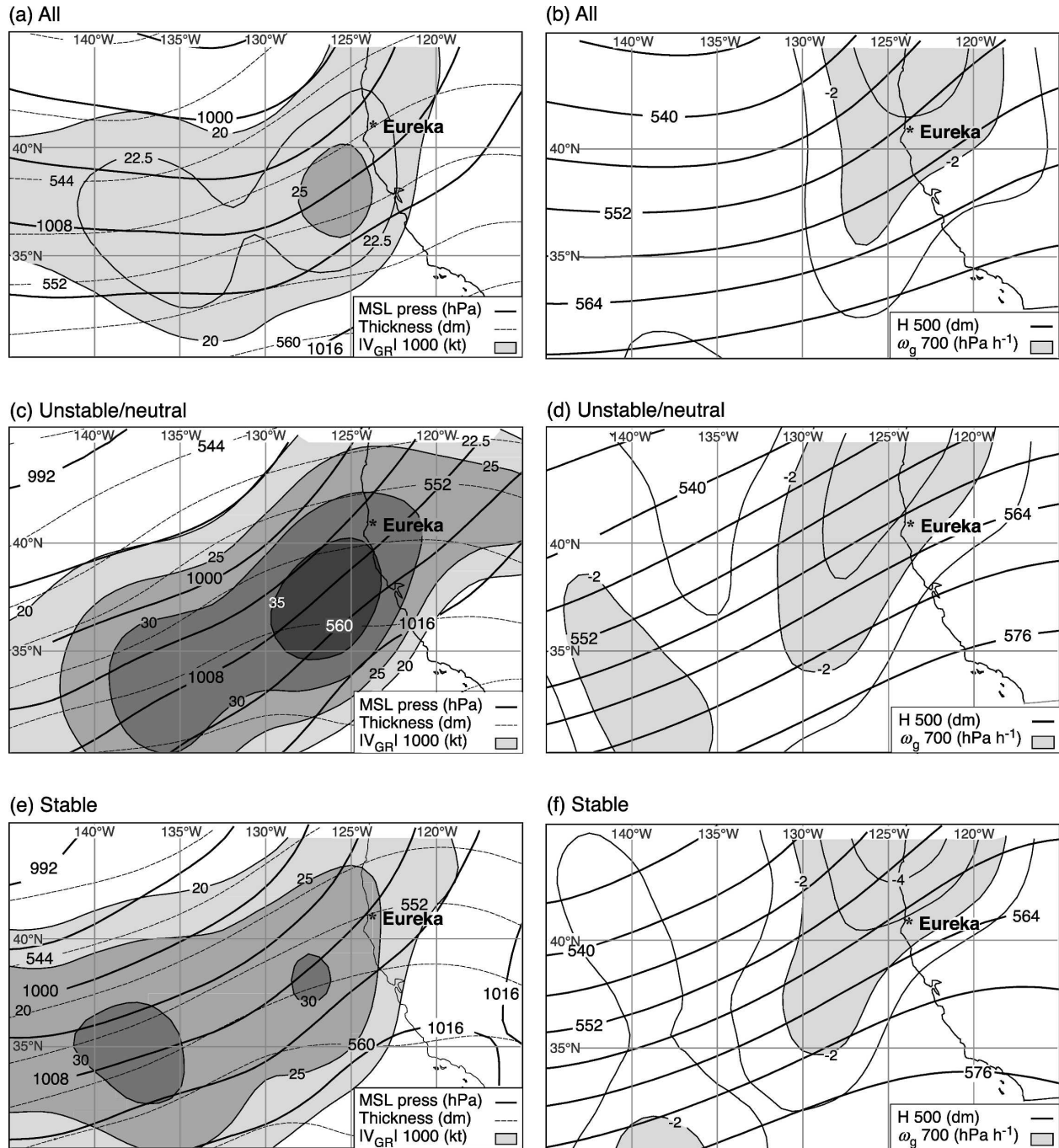
FIG. 4. Mean NCEP reanalysis fields, averaged over 60 heavy-precipitation events during 1 Oct 1995–31 Mar 1998. (a) MSL pressure, 1000–500-hPa thickness, and isotachs of gradient wind; (b) 500-hPa height and ω; (c) and (d) composite synoptic patterns for the subset of heavy-rain events that had unstable or neutral west-southwesterly flow in the 900–800-hPa layer, with the 0°C level above 2.5 km MSL; and (e) and (f) same as (c) and (d), respectively, except that only stable events are shown.

are both elongated in Figs. 4d and 4f, with apparent frontal orientation from south-southwest to north-northeast. In both cases, the California coast appeared to be located in prefrontal flow.

Figure 5a shows the overall mean upstream sounding at 50-hPa vertical resolution derived from the Eta Model analysis and 6-h forecast fields (section 2) for the 61 heavy-precipitation days. The average 0°C level is around 780 hPa (2.1 km MSL), and the −15°C level is about 560 hPa (~4 km MSL). The dewpoint depression

in the profile gradually increases from about 2°C at the surface to 8°C above 4 km MSL, indicating that midlevel cloud was less frequent than at low levels. In addition, the temperature profile reveals the prevalence of weak conditional instability below the 850-hPa level, combined with abundant near-surface moisture. Within the layer of conditional instability below 850 hPa, the wind profile veered with height, indicative of warm advection and/or Ekman turning, with an average 900–800-hPa wind speed of 30–35 kt ($\sim$15–18 m s^{-1}) from the west-southwest. The mean Eta-derived profile in Fig. 5a is consistent with the point dropsonde observations of Ralph et al. (2005) within 17 different landfalling LLJs, except that the larger area sampling in our Eta Model profile depicts slight conditional instability rather than moist neutrality in the 900–800-hPa layer and dry air intrusion at midlevels.

Figure 5b shows the average sounding for the unstable/neutral events, while Fig. 5c shows the average sounding for the stable events. A small but notable difference between the stable and unstable events is that the stable events (Fig. 5c) had higher humidity (indicated by much smaller dewpoint depression values) at midlevels. As will be shown, the intensity of the orographic modification of the synoptic-scale precipitation pattern was sensitive to these slight differences in stability and/or humidity.

4. Radar climatology

The horizontal cross sections of echo patterns described in this section are mostly taken at the 2-km level, which is high enough to avoid much of the near-field blocking of the radar beam by the terrain while being in the rain layer below the 0°C level (Fig. 2). Vertical cross sections incorporate all available grid levels.

Figure 6a shows the 2-km-altitude horizontal display of reflectivity over coastal northern California, averaged over the 61 heavy-precipitation days. Partial beam shadowing occurred behind South Fork Mountain (Fig. 1) and other terrain features, and corresponding radar gates beyond those obstacles to the beam were removed from the dataset. Removal of these blocked and partially blocked beams results in the circle of radar observations being much smaller to the east of the ra-
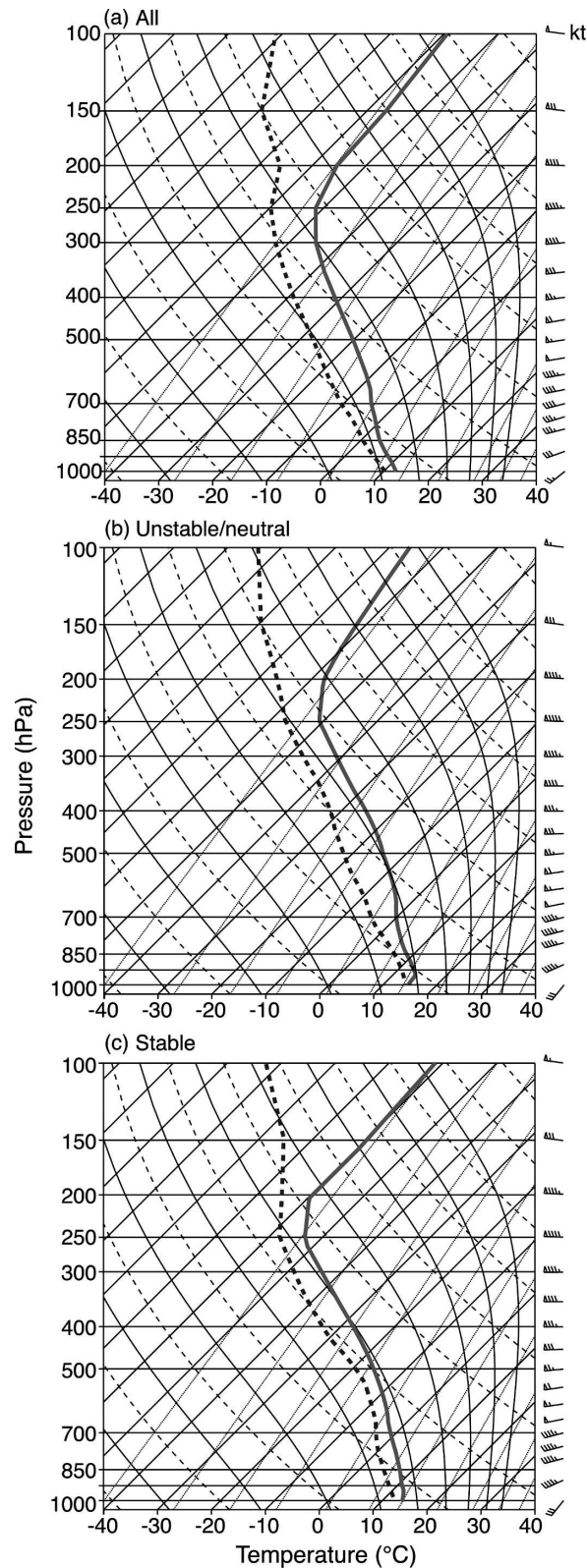
FIG. 5. Mean upstream soundings (location shown in Fig. 1) derived from Eta Model output. (a) The average over all 60 heavy-precipitation days. (b) and (c) Mean soundings for subsets of days with west-southwesterly flow at 900–800-hPa flow and 0°C level above 2.5 km MSL. The temperature profile is solid, and the dewpoint temperature is dashed.
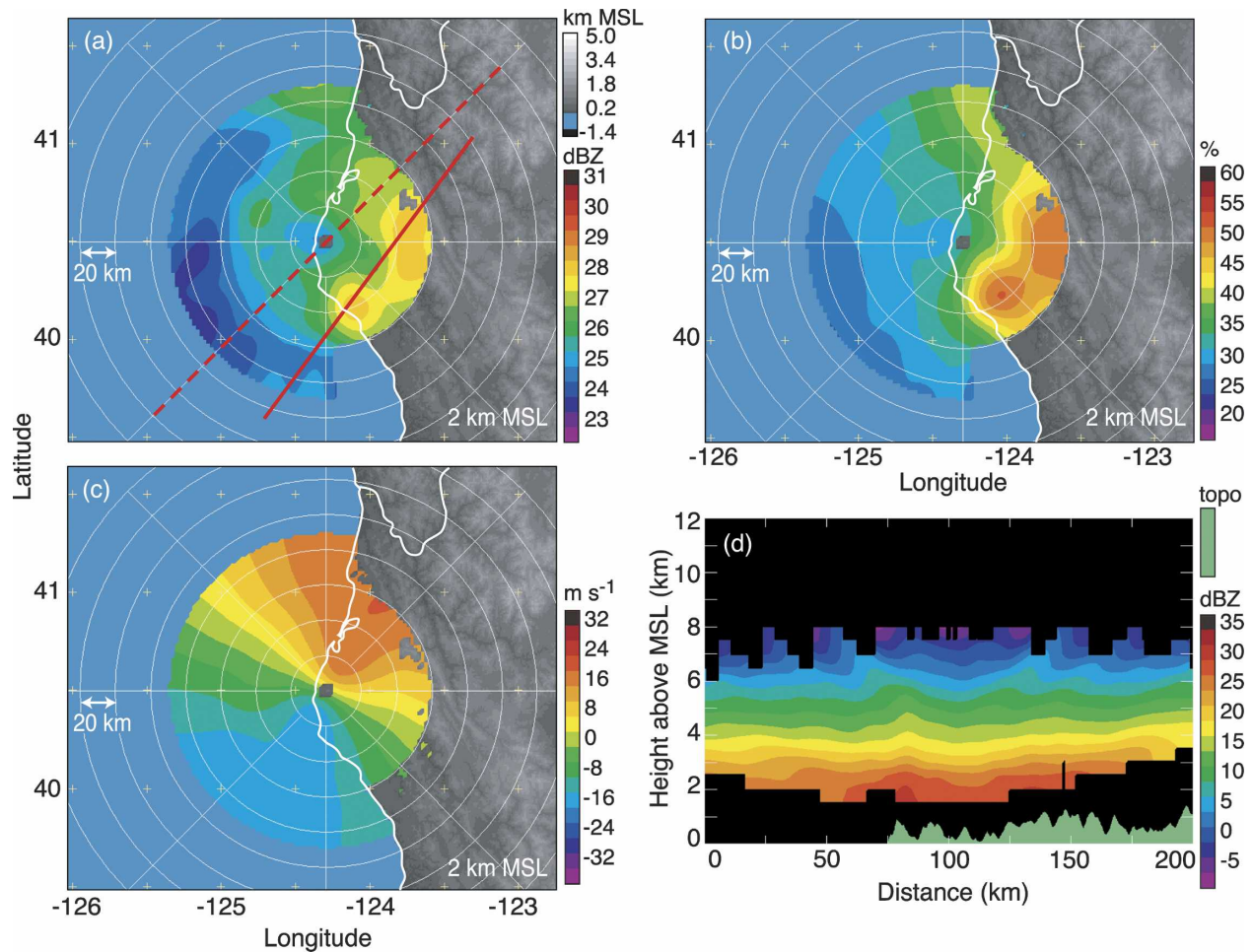
FIG. 6. Radar-derived precipitation climatology obtained for all heavy-precipitation events observed by the Eureka WSR-88D, comprising a total of 1176 hourly radar volumes. Constant altitude plots of 2 km depict (a) mean reflectivity, (b) the rainfall frequency, or percentage of radar volumes in which the reflectivity was at least 13 dBZ, and (c) mean Doppler radial velocity. Negative (positive) radial velocity indicates flow toward (away from) the radar. Range ring spacing is 20 km, and azimuth lines are drawn every 45°. The white contour represents the coastline. (d) A vertical cross-section plot of mean reflectivity from southwest to northeast along the solid red line in (a), with the underlying terrain shaded green. The dashed red line in (a) indicates the position of vertical cross sections in Fig. 7.

dar than to the west in Fig. 6 and similar figures throughout the paper.

The overall pattern of reflectivity in Fig. 6a indicates both enhancement of echo directly over the coastal mountains and upstream of the coastline. The enhancement over the terrain is evident from the echo maxima over the King Range and over the crest and windward slopes (southwest side) of South Fork Mountain and the immediately adjacent terrain to its south (locations in Fig. 1), while upstream enhancement of the precipitation processes is evident from the echo pattern over the ocean.

The echo contours offshore are oriented roughly parallel to the coast, with echo intensity generally increasing toward shore. The strongest offshore gradient of

reflectivity is roughly 60 km from the coastline, which is roughly 150 km from the crest of the Coastal Range. Estimates of the Rossby radius ($L = NH/f$) using the representative dry Brunt–Väisälä frequency ($N = 0.01$ s^{-1}), characteristic terrain height ($H = 1.5$ km MSL), and Coriolis parameter $f = 10^{-4}$ s^{-1} correspond to this offshore distance, suggesting that convergent lifting due to geostrophic adjustment in subcloud air may be enhancing precipitation upstream, before the southwesterly airstream (Fig. 6c) directly encounters the coastal terrain. The Rossby radius estimated using a moist Brunt–Väisälä frequency (Durran and Klemp 1982) characteristic of absolutely stable events ($N = 0.002$ s^{-1}) is only about 30 km, and within this distance from the barrier the reflectivity was even higher, suggesting

additional adjustment within the cloud layer itself, closer to shore. However, these are only rough estimates. The Doppler velocity data do not provide conclusive evidence of the suspected upstream flow adjustment, and the complexity of the terrain and variability in the static stability make scale analysis to obtain the appropriate expression of the Rossby radius problematic.

A quasi-circular maximum of reflectivity is apparent offshore at a radar range of about 40 km in Fig. 6a. This curved maximum is associated with the brightband effect of melting ice particles. However, the ringed pattern also mimics the shape of the coastline, which bulges westward at Cape Mendocino, and the curved reflectivity pattern could therefore also indicate upstream enhancement of the precipitation. Braun et al. (1997) analyzed aircraft data and found that the upstream modification of echo patterns appeared as an echo maximum paralleling the Pacific coastline.

Figure 6a shows that maxima of the mean reflectivity occurred over specific areas of the terrain, especially over the King Range and South Fork Mountain (Fig. 1). The question arises whether the precipitation was more intense or more frequent in these locations. Figure 6b depicts the percentage of radar volumes in which the reflectivity equaled or exceeded 13 dBZ, which is roughly equivalent to a rainfall rate of 0.2 mm h^{-1}. Overall, the patterns in Figs. 6a and 6b are qualitatively similar, suggesting that orographic forcing generally makes the precipitation *more frequent* rather than *more intense*. (An exception to this rule will be discussed in section 7b.) Calculations of mean conditional rainfall rate (not shown), which is related to mean echo intensity, confirm this result, with the exception that slightly higher echo intensity occurred both over the higher terrain and offshore within roughly 60 km of the coast.

Figure 6c shows the prevailing Doppler velocity at 2 km MSL, averaged over all 1176 radar volumes. The mean flow was nearly perpendicular to the Coastal Range from the southwest at speeds approaching 20 m s^{-1} at 2 km MSL. Maps of the Doppler velocities at other altitudes indicated that the wind was veering with height, especially below 3-km-MSL altitude, consistent with frictional turning, flow blocking, and/or warm advection. The strong horizontal low-level wind toward the coast in the storms examined in this study (~20 m s^{-1}) was at least twice the strength of the cross-barrier low-level wind component of ~8 m s^{-1} observed during heavy-rainfall events in the Alps during MAP (see HJM). The mean soundings (Fig. 5) show that the strong flow toward the barrier in the 1–3-km (900–700 hPa) layer during heavy-precipitation events had Froude numbers greater than unity for both satu-
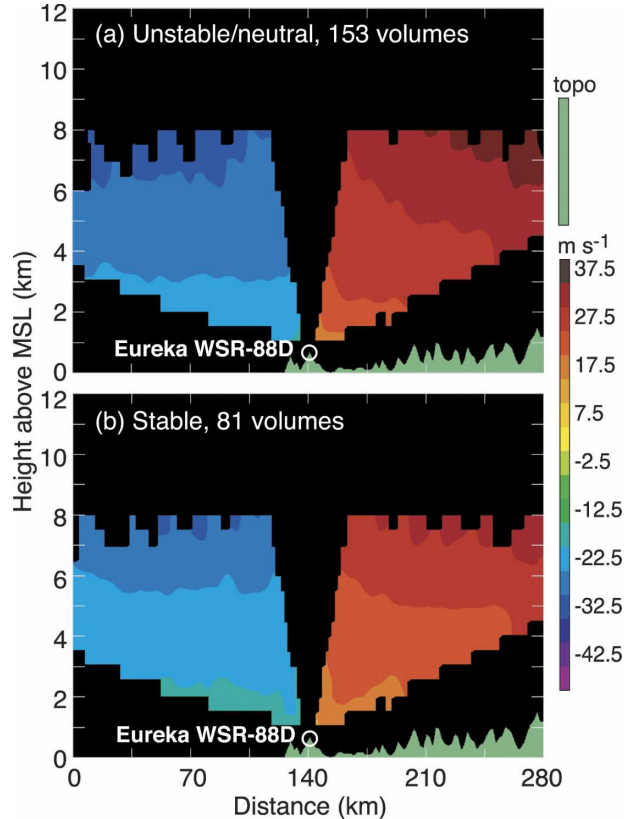

FIG. 7. Vertical cross sections of mean radial velocity during (a) unstable/neutral and (b) stable events (analysis V) taken approximately parallel to the wind along the dashed red line in Fig. 6a. The terrain is shaded green, and negative (positive) radial velocity indicates flow toward (away from) the radar location shown at 140-km distance and 767-m altitude.

rated and unsaturated air, indicating that flow blocking was not occurring at these levels. Figure 7 shows the average Doppler radial velocity along a southwest–northeast cross section passing through the radar site for unstable/neutral and stable conditions (as defined in section 3). Both sections show strong southwesterly flow increasing gradually with height throughout the layer observed by the radar. The flow was slightly less intense in the stable cases but nevertheless rapidly moving over the coast and up over the mountains. These sections are, again, consistent with unblocked flow above the 1-km level.

The vertical cross section of average reflectivity in Fig. 6d, taken parallel to the prevailing southwesterly wind along the red line in Fig. 6a is consistent with unblocked flow over the coastal terrain. A maximum of echo intensity occurred over the first major peak of terrain (i.e., the King Range, located at about 70 km on the horizontal scale in Fig. 6d). This maximum extended to the higher levels as an upward protrusion of

the reflectivity contours over the first peak. A similar echo structure is seen in the radar echo climatology of unblocked flow cases on the Mediterranean side of Alps (HJM; Medina and Houze 2003). A secondary maximum of reflectivity occurred in the cross section over the second major rise of terrain (120–150 km on the horizontal scale in Fig. 6d). The echo contours over land slope upward in the same sense as the generally increasing height of the terrain at distances greater than 110 km in Fig. 6d. This upward-sloping aspect of the echo contours over the terrain indicates a general orographic enhancement of the precipitation-formation processes over the windward slopes of the coastal mountains. This type of enhancement is consistent with unblocked flow, and it will be shown below that this upward slope of contours is more pronounced when the cross-barrier wind component is stronger and when the static stability of the upstream flow is reduced. Echo features embedded within the general echo pattern over the terrain are also consistent with unblocked flow.

Despite the overwhelming evidence for unblocked flow above the 1-km level in both the sounding data (Fig. 5) and the radar data just discussed, upstream precipitation enhancement was noted in Fig. 6a and is also evident in the offshore portion of the vertical cross section in Fig. 6d. Such upstream precipitation enhancement is often associated with low-level flow blocking (e.g., Grossman and Durran 1984; HJM; Medina and Houze 2003). However, in the case of frontal systems approaching a coastal mountain barrier, the dynamics of frontogenesis is enhanced in the offshore coastal zone (Yu and Smull 2000; Colle et al. 2002; Olson and Colle 2004). Enhanced frontogenesis immediately offshore could therefore account for the offshore precipitation enhancement while unblocked flow over the mountains accounts for precipitation over the land.

However, blocking offshore cannot be ruled out as an explanation for the echo enhancement seen in the echo climatology over the ocean upstream from the coastal mountains. Because the Eureka radar is located on a mountain (767 m MSL), radar data for the major rain events considered here do not extend below the 1-km level close to the radar, or below 3 km far from the radar. It is therefore impossible to know the reflectivity or radial velocity conditions in the boundary layer or near the sea surface, and we can only speculate about what happens at these very low levels. The echo enhancement upstream of the coastal mountains could have been influenced by a very thin (<1 km deep) layer of near-surface air, in contact with the cold ocean and/or dammed against the coastal terrain. Neiman et al.

(2002, 2004) have found such a thin layer of cool stable air off the coast of California and have suggested that it was associated with blocking and modification of land-falling cyclones with southwesterly LLJs of the type prevalent in the cases we are considering here. The landward-moving air seen above the surface layer could have been lifted upstream over this shallow layer of cold air. Lifting of the upper layer over the lower cool layer could provide sufficient upward mass transport and condensation to produce the observed offshore echo enhancement. The layer of air overriding the thin layer of cool air over the ocean could have then proceeded inland and further risen over the coastal mountains in a relatively unblocked fashion. This behavior would explain why upstream echo enhancement of the type associated with blocked flow occurs offshore even though the soundings and radar data above the 1-km level exhibit unblocked flow characteristics. Thus, the echo enhancement upstream of the mountains could be produced either by flow rising over a thin cold pool dammed against the coastal mountains or by coastal-zone enhancement of frontogenetic processes in the landfalling baroclinic systems.

5. Epochs

We performed many superimposed epoch analyses to investigate the sensitivity of the coastal orographic precipitation enhancement to characteristics of the upstream low-level (900–800 hPa) and midlevel (700–500 hPa) flow. In the MAP studies of Alpine precipitation, HJM and Medina and Houze (2003) found that the radar data grouped distinctly according to the Froude number F of the flow [where $F = U/(Nh)$, U is the speed of the wind normal to an idealized two-dimensional barrier of height h, and N is either the moist or dry Brunt–Väisälä frequency]. In the present study, however, we find that the radar data in the vicinity of the northern California coastal mountains had low correlation with the Froude number of the upstream 900–800-hPa layer. A difference between the Alpine cases and the northern California coastal cases is that in the Alps, the flow over the terrain was not directly associated with the front, which was usually on the northwestern side of the Alps. Moist flow from the Mediterranean impinged on the Alpine barrier without frontal effects, and the ocean was quite far upstream of the barrier. In northern California, frontogenetic effects in the coastal zone (Yu and Smull 2000; Colle et al. 2002; Olson and Colle 2004) and possibly a shallow layer of stable air over the cold water immediately in front of the coastal mountains produced effects not present in the Alpine cases. These effects apparently led to upstream en-

TABLE 2. Superimposed epoch analyses. Shown are the criteria used to separate the WSR-88D archive into epochs for superimposed analyses I–V. Also tabulated are the number of hourly radar volumes used for each analysis and all corresponding figures (FZL = freezing level).

Analysis	Epoch 1	Epoch II	Epoch III	Epoch IV
I. 900–800-hPa wind direction	180°–210°	210°–240°	240°–270°	270°–300°
	54 volumes	330 volumes	362 volumes	235 volumes
	Fig. 8a	Fig. 8b	Fig. 8c	Fig. 8d
II. 700–500-hPa wind speed (low-level wind direction 225°–270°; FZL ≥ 2.5 km)	0–30 m s^{-1}	30 m s^{-1}–∞		
	125 volumes	103 volumes		
	Figs. 9a,b	Figs. 9c,d		
III. 700–500-hPa dewpoint depression (low-level wind direction 225°–270°; FZL ≥ 2.5 km)	3°C–∞	0°–3°C		
	104 volumes	124 volumes		
	Figs. 10a,b	Figs. 10c,d		
IV. 900–800-hPa wind speed (low-level wind direction 225°–270°; FZL ≥ 2.5 km)	0–20 m s^{-1}	20 m s^{-1}–∞		
	104 volumes	130 volumes		
	Figs. 13a,b	Figs. 13c,d		
V. 900–800-hPa moist Brunt–Väisälä frequency (low-level wind direction 225°–270°; FZL ≥ 2.5 km)	Imag.–0 s^{-1}	0 s^{-1}–∞		
	153 volumes	81 volumes		
	Figs. 3c,d; 4b; 14a,b; 7a; 16a	Figs. 3e,f; 4c; 14c,d; 7b; 16b		

hancement of precipitation in addition to the enhancement associated with unblocked upslope flow directly over the mountains. In this case, the echo pattern would not be expected to correlate simply with *F*. The superposed epoch analyses show instead that, to a first approximation, the radar echo patterns tended always to be similar, regardless of the observed flow strength and stability. The echo patterns in the various data groupings generally resemble the mean patterns in Fig. 6. However, the various features of the mean echo fields seen in Fig. 6 vary in degree depending on the strength of the cross-barrier flow, the upstream stability, and the degree of saturation prevailing in the cloud layers of the storms passing over the coastal mountains.

Table 2 lists the upstream flow characteristics that will be presented hereafter in this paper. For brevity, only those superposed epoch analyses connected with substantial variations in the observed radar echo fields have been included. These characteristics are subdivided into low-level and midlevel flow features. The radar volumes were divided into "analysis" subsets based on environmental variables as shown in Table 2. Within each analysis subset (labeled I–V), the data are subdivided into "epochs" of interest.

Analysis I indicates how the mean radar echo field varies according to the prevailing low-level wind direction. Figure 8 displays horizontal cross sections of the mean reflectivity composites when the offshore low-level layer-averaged wind direction was (a) south-southwesterly (180°–210°), (b) southwesterly (210°–240°), (c) west-southwesterly (240°–270°), and (d) west-northwesterly (270°–300°). In this figure, it is evident that each low-level flow direction had at least some

precipitation enhancement over South Fork Mountain and the King Range (Fig. 1).

Figure 8a shows the southerly to south-southwesterly epoch. The overall intensity of echo in this epoch was much greater than those shown in the other three echo panels. However, it was based on a much smaller sample of volumes, 54 compared to 330, 365, and 235 in the other three panels. This sample may not be representative of all cases with this wind direction. On the other hand it may indicate that this rare type of case has particularly heavy rainfall. In any case, the sample is not large enough for further analysis.

Of primary interest are the epochs represented in Figs. 8b and 8c, which are based on a large number of volumes and which represent wind directions orthogonal to the ridgelines of the coastal mountains. These southwesterly wind directions typify the LLJs of California baroclinic storms of the type described by Ralph et al. (2004) and others. This flow brought plentiful moisture into the region (Ralph et al. 2004) and typically possessed a higher static stability. Precipitation was enhanced both by the mountains over land and well upstream, as was seen in the overall average reflectivity patterns for all heavy-rain events (Fig. 6a).

Figure 8d represents west-northwesterly low-level flow, which was likely postfrontal and therefore less stable. This regime exhibited lower-than-average mean reflectivity values over most of the domain and especially over the ocean, upstream of the coastal terrain. These flow directions provided less moisture and lower static stability, and therefore favored less upstream blocking and more intermittent convective showers directly over the terrain. The mean radar reflectivity pat-
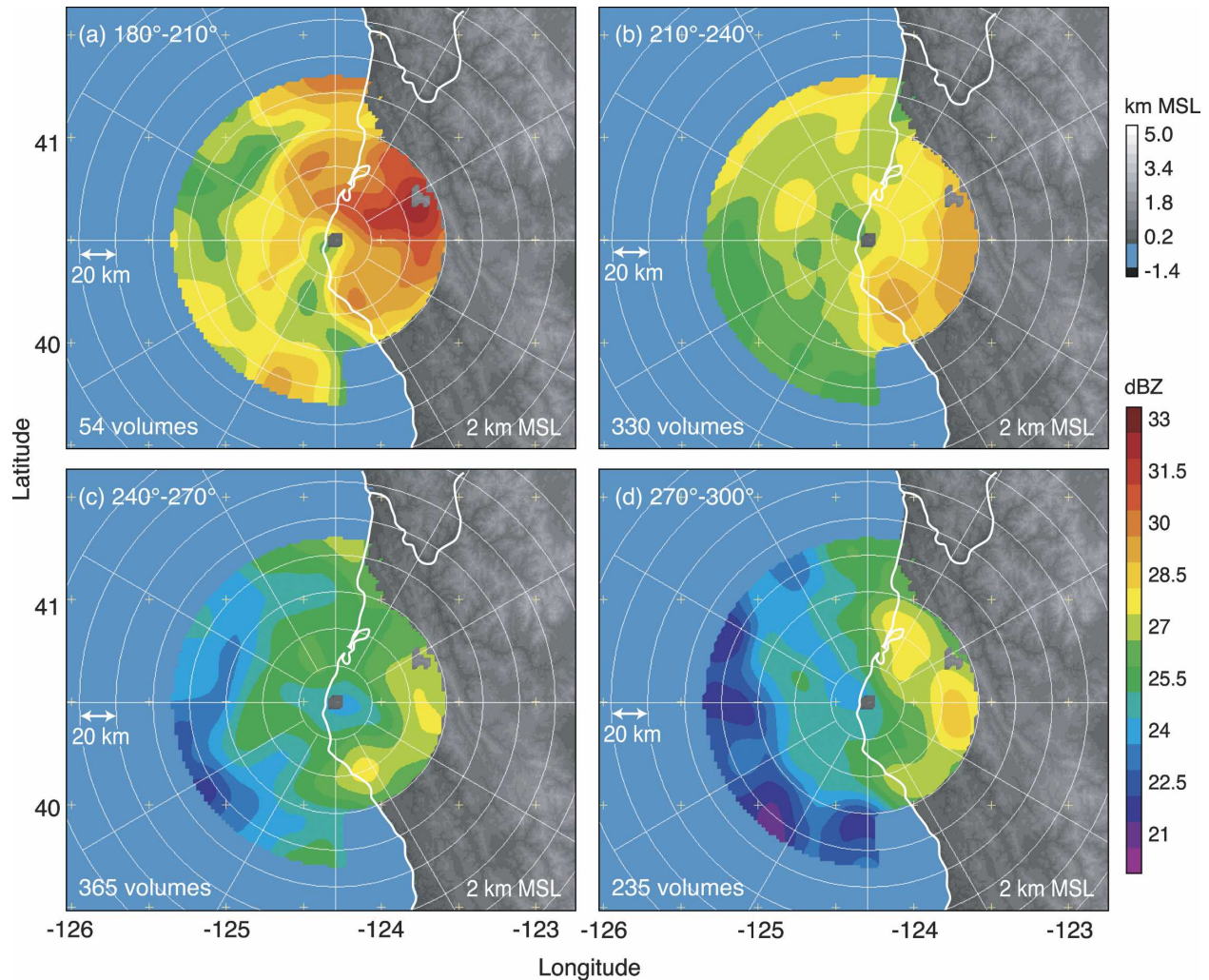
FIG. 8. Superimposed epoch analysis of mean reflectivity at an altitude of 2 km MSL when the 900–800-hPa flow direction upstream was (a) south-southwesterly, (b) southwesterly, (c) west-southwesterly, and (d) west-northwesterly. Range ring spacing is 20 km with azimuth lines drawn every 30°.

tern under these conditions exhibited the same general upslope enhancement as the southwesterly cases. However, the enhancement was more evident in the coastal mountains north of the radar and reduced to the south of the radar in response to the more reduced southerly component of flow and increased westerly component. A brightband ring pattern at 60-km range from the radar is apparent in both Figs. 8c and 8d, consistent with lower 0°C levels in the colder postfrontal air when the flow became more westerly.

In the remainder of the paper, we will restrict the discussion to the set of echo volumes for which the low-level (900–800 hPa) wind directions were 225°–270°. These directions fall within the southwesterly–westerly epochs of Figs. 8b and 8c but are restricted to the directions most orthogonal to the coastal mountain

ranges and hence most likely to produce strong orographic precipitation enhancement. The results in the remainder of the paper are further restricted to cases for which the 0°C level was at least 2.5-km-MSL altitude. Constraining the height of the 0°C level in this way minimized brightband contamination of the echo patterns in the 2-km-MSL horizontal displays.

6. Relationship of radar climatology to midlevel flow

a. Analysis II: Midlevel wind speed

The strength of the midlevel (700–500 hPa) flow is an indication of the strength of the large-scale baroclinic forcing. Figure 9 shows the mean reflectivity at 2-km-MSL altitude as a function of the 700–500-hPa layer-
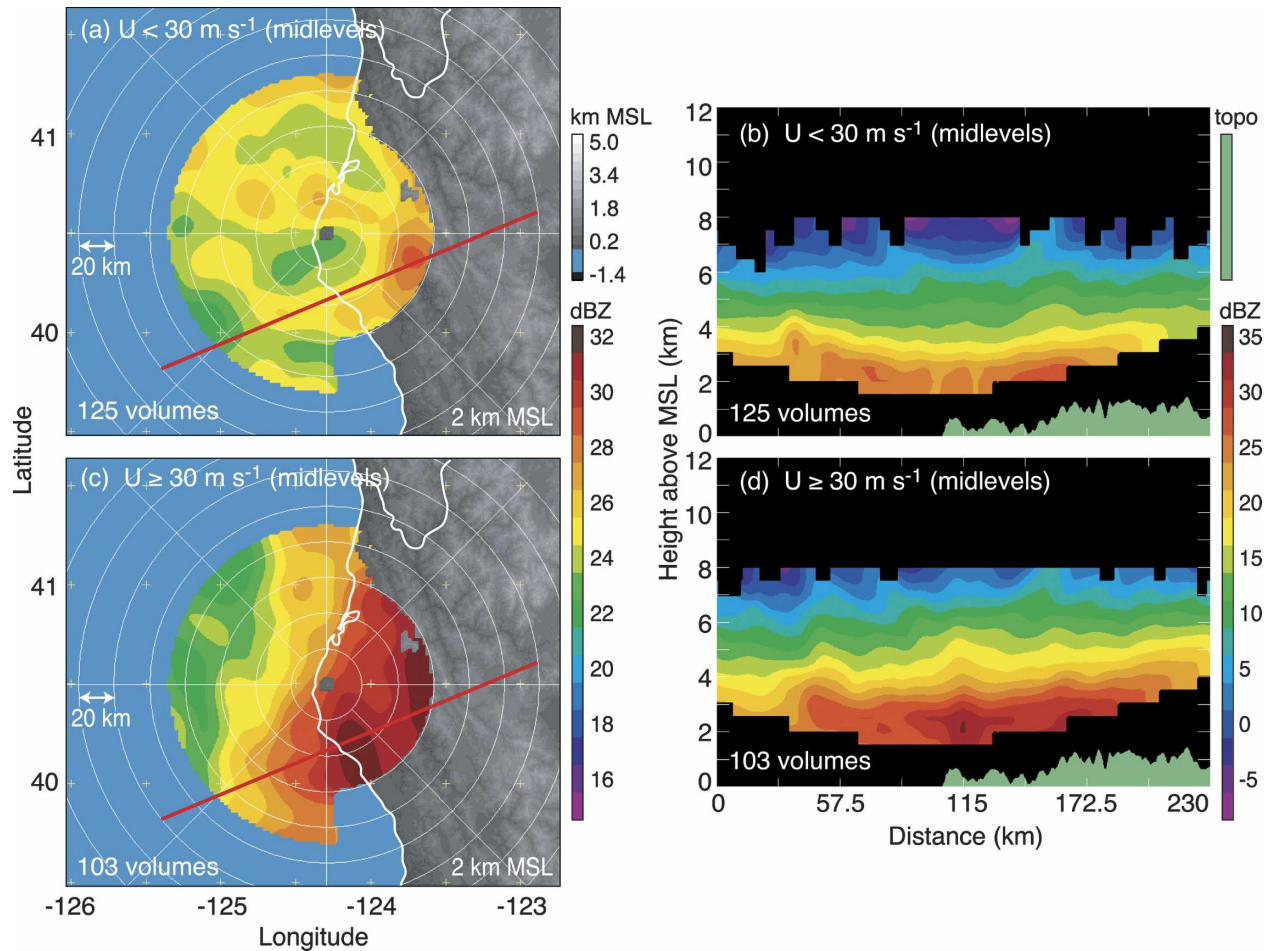
FIG. 9. For the subset of radar volumes in which the 900–800-hPa wind direction fell between 225° and 270° and the 0°C level was at least 2.5 km, this analysis shows the mean reflectivity at 2 km MSL when the layer-averaged 700–500-hPa wind speed was (a) less than 30 m s^{-1} and (c) at least 30 m s^{-1}. (b) and (d) Vertical cross sections of mean reflectivity from west-southwest to east-northeast along the red lines in (a) and (c), respectively, with the underlying terrain profile shaded green. Range ring spacing is 20 km with azimuth lines drawn every 45°.

averaged wind speed. When the midlevel wind speed was weaker (<30 m s^{-1}; Fig. 9a), the echo enhancement over the coastal mountains was evident, but the mean echo pattern had a somewhat random character offshore. The vertical cross section of reflectivity in Fig. 9b lies along the red line in Fig. 9a, which is generally parallel to the LLJ. The offshore upstream echo enhancement produced an upward-protruding mean echo at a horizontal distance of about 35–40 km.

The greatest echo enhancement was at low levels over the windward slopes, midway up the range (Fig. 9b; $x = 130$–170 km). The maximum echo over the first peak of terrain was apparent but weaker than average (cf. Fig. 6d). The echo core at the leading edge of the offshore enhanced echo region was evident as an upward protrusion of the echo contours at ~35–40 km on the horizontal distance scale. Proceeding shoreward,

the echo contours drop in height to a minimum near the coast. Progressing inland, the echo contours slope upward in apparent response to orographic lifting over the windward slopes of the coastal mountains. The echo enhancement at lower levels over land (as seen in the 25–30-dBZ filled contours) exhibits local maxima over both the King Range and South Fork Mountain ridges (Fig. 1).

Stronger midlevel wind speed ($\geq$30 m s^{-1}) produced a much stronger and less noisy pattern of radar echo enhancement (Fig. 9c). This epoch shows clearly all the orographic effects on the baroclinic precipitation seen in the mean pattern (Fig. 6a), thus indicating the strong role of the cross-barrier flow strength in the orographic modification of the precipitation processes. The offshore echo intensity gradient associated with upstream enhancement was strong and sharply defined, and the
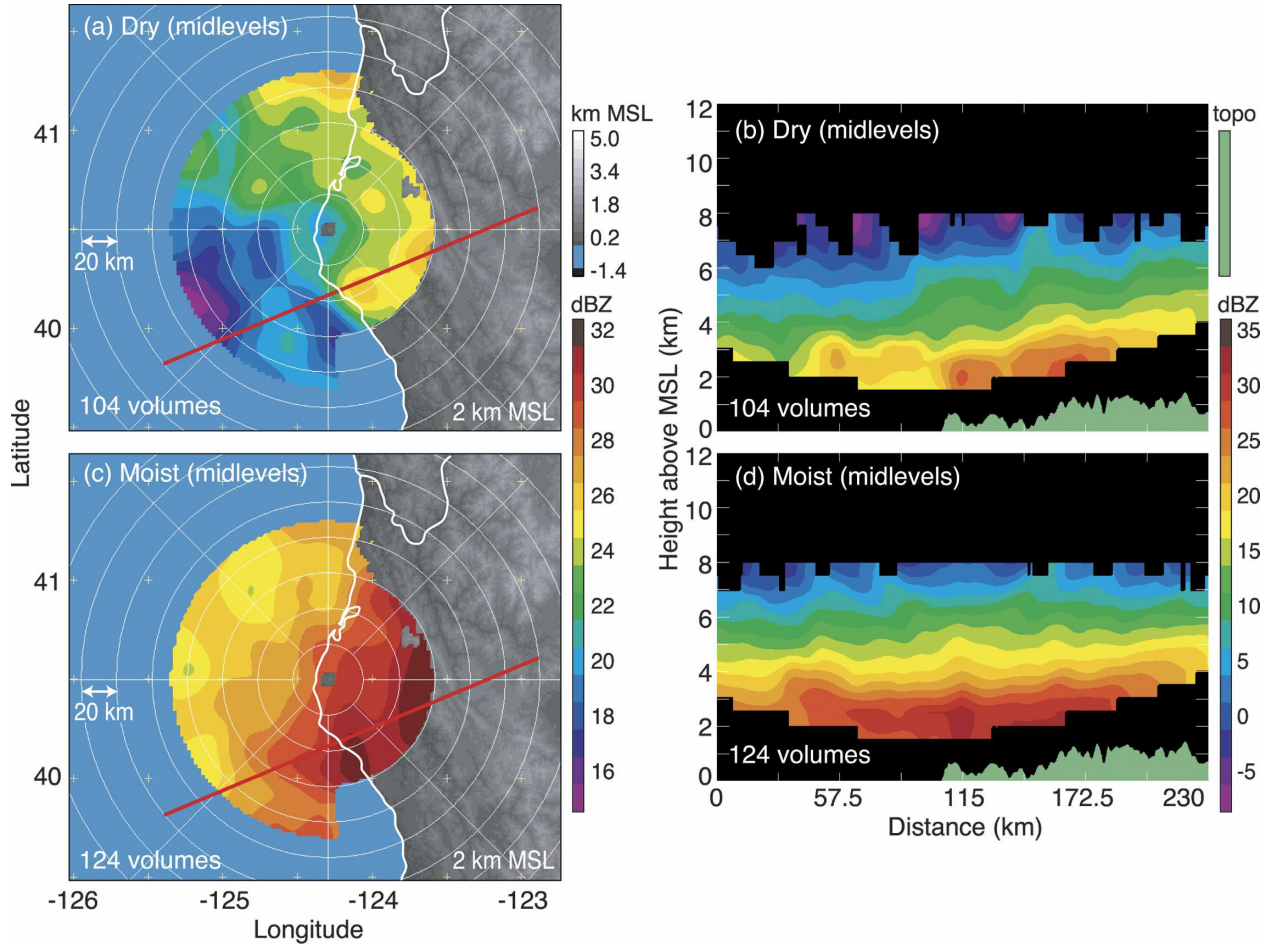
FIG. 10. As in Fig. 9, with the exception that the mean reflectivity is depicted for those events when the 700–500-hPa layer-averaged dewpoint depression was (a) at least 3°C and (c) less than 3°C. (b) and (d) Vertical cross sections respective to (a) and (c).

echo intensity directly over the first two primary ridges in the terrain was greatly intensified. The strong upstream enhancement began ~50–60 km offshore.

Figure 9d shows the bright band clearly both just ahead of and just downstream from the first peak of terrain. The bright band emphasizes the broad stratiform nature of the precipitation. Over land the echo contours slope upward in concert with the mean rise of the terrain, indicating a general upslope enhancement of the precipitation as the strong cross-barrier winds rose over the terrain. The broad stratiform pattern was punctuated by strong mean upward-protruding echo cores at the leading edge of the offshore upstream enhancement (~40–50 km on the horizontal distance scale), over the first peak of terrain (King Range at ~115 km), and to a lesser extent over the second major rise of terrain (South Fork ridge at ~160–170 km). In this well-defined pattern, the precipitation extrema over individual peaks (especially over the King Range) were apparently displaced downwind from their posi-

tions in Fig. 9b by the stronger midlevel flow. Precipitation was thus more apt to spill over into inland areas of the stronger midlevel cases. The stratiform precipitation marked by the strong bright band in the offshore region possibly was enhanced by ice particles advected from the upper portion of the upward-protruding echo core at the leading edge of the offshore enhancement zone, analogous to a trailing stratiform region following a squall line (e.g., Houze et al. 1989).

b. Analysis III: Midlevel dewpoint depression

The importance of midlevel humidity to the orographic precipitation enhancement is indicated by the Eta Model 700–500-hPa dewpoint depression (temperature minus dewpoint) of the midlevel flow (Fig. 10). The greater the dewpoint depression at these levels, the better developed are the midlevel clouds of the baroclinic storm system passing over the coastal mountain ranges. The lower humidity upstream implies that the cloud layer developing over the mountains would

have lower condensed water content since some of the lifting would be used to saturate the air prior to condensation. A weakly developed cloud layer might contain layers of unsaturated air. In the lower humidity (dewpoint depression >3°C), much lower reflectivity was generally observed; however, all the main orographic precipitation features remained intact (Figs. 10a and 10b). The vertical cross section (Fig. 10b) shows the echo core at the leading edge of the offshore enhancement zone, the bright band offshore downwind of the leading core, the local echo maxima over and slightly downwind of the first and second major rises of terrain, and the overall upward slope of the contours over the windward slopes of the coastal mountains. When the midlevel dewpoint depression was <3°C, indicating that the midlevel clouds of the passing storm system were well developed, all the same orographic precipitation features were evident in the cross section (Fig. 10d), but they were all more intense. Figures 9c,d and 10c,d together demonstrate that the strength of the large-scale midlevel flow and the humidity (i.e., degree of cloud development) were the two primary controlling factors over the intensity of the orographic precipitation features appearing upstream and over the coastal mountains at midlevels in the baroclinic system passing over the mountains.

7. Sensitivity of heavy precipitation to low-level flow characteristics

a. Analysis IV: Low-level wind speed

Heavy-precipitation events over the coastal mountains of northern California are associated with a southwesterly LLJ (Ralph et al. 2004). To analyze the response of the radar reflectivity field to the strength of the LLJ, we examine the radar volumes in the heavy-precipitation events that had low-level wind directions of 225°–270° and 0°C level at or above 2.5 km MSL. These criteria included nearly one-quarter (234) of the radar volumes in heavy-precipitation events (Fig. 11) and segregated those events for which the low-level wind was approximately orthogonal to the ridges of the Coastal Range (Fig. 1). Figure 12 shows that most of the radar volumes with wind directions of 225°–270° had LLJ speeds between 15 and 25 m s^{-1}. In this section, we analyze the response of the radar reflectivity field to the strength of the LLJ by subdividing the dataset into epochs according to whether the 900–800-hPa wind speeds were < or ≥20 m s^{-1} (Fig. 13).

In the weaker low-level wind epoch (Fig. 13a), the reflectivity pattern was overall somewhat weaker and differed in some details from the stronger low-level wind epoch (Fig. 13b). Nonetheless, the vertical cross
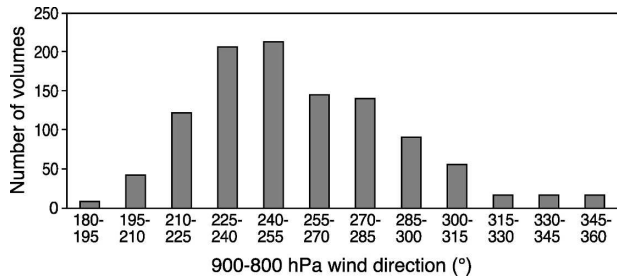

FIG. 11. Histogram of the frequency of occurrence of average wind direction in the 900–800-hPa layer expressed as the number of hourly WSR-88D volumes in the radar archive corresponding to the indicated wind direction (°).

sections in Figs. 13b and 13d both exhibit the same basic structure seen in Figs. 6d, 9d, and 10d. Widespread stratiform precipitation extended across the region of the cross section, with a bright band evident both upstream and downstream of the coast. The bright band was better defined when the flow was stronger, and the generally upward-sloping reflectivity contours over the inland terrain indicate that the stratiform precipitation was being enhanced by the forced ascent on the scale of the broadscale mountain barrier. As in previous cross sections, the stratiform echo pattern was punctuated by upward bulges of the reflectivity contours over the first and second major peaks of the terrain (the King Range at 110 km on the horizontal distance scale and the South Fork Mountain ridge at 160 km).

As in Figs. 6d, 9d, and 10d, upstream echo enhancement is seen out to ~40 km from shore in Figs. 13b and 13d. An upward protrusion of echo at the leading edge of the offshore enhanced echo region in both Figs. 13b and 13d suggests an abrupt rise of the air at that distance offshore, perhaps indicating the onshore low-level flow was bumped upward over a thin surface layer of denser air. This behavior would support the idea that
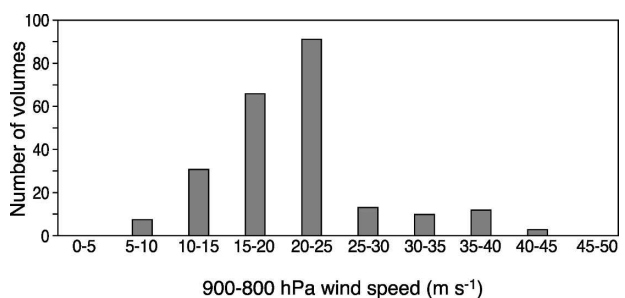

FIG. 12. Histogram of the frequency of occurrence of average wind speed in the 900–800-hPa layer expressed as the number of hourly WSR-88D volumes in the radar archive corresponding to the indicated wind speed (m s^{-1}). Only cases for wind directions of 225°–270° are included.
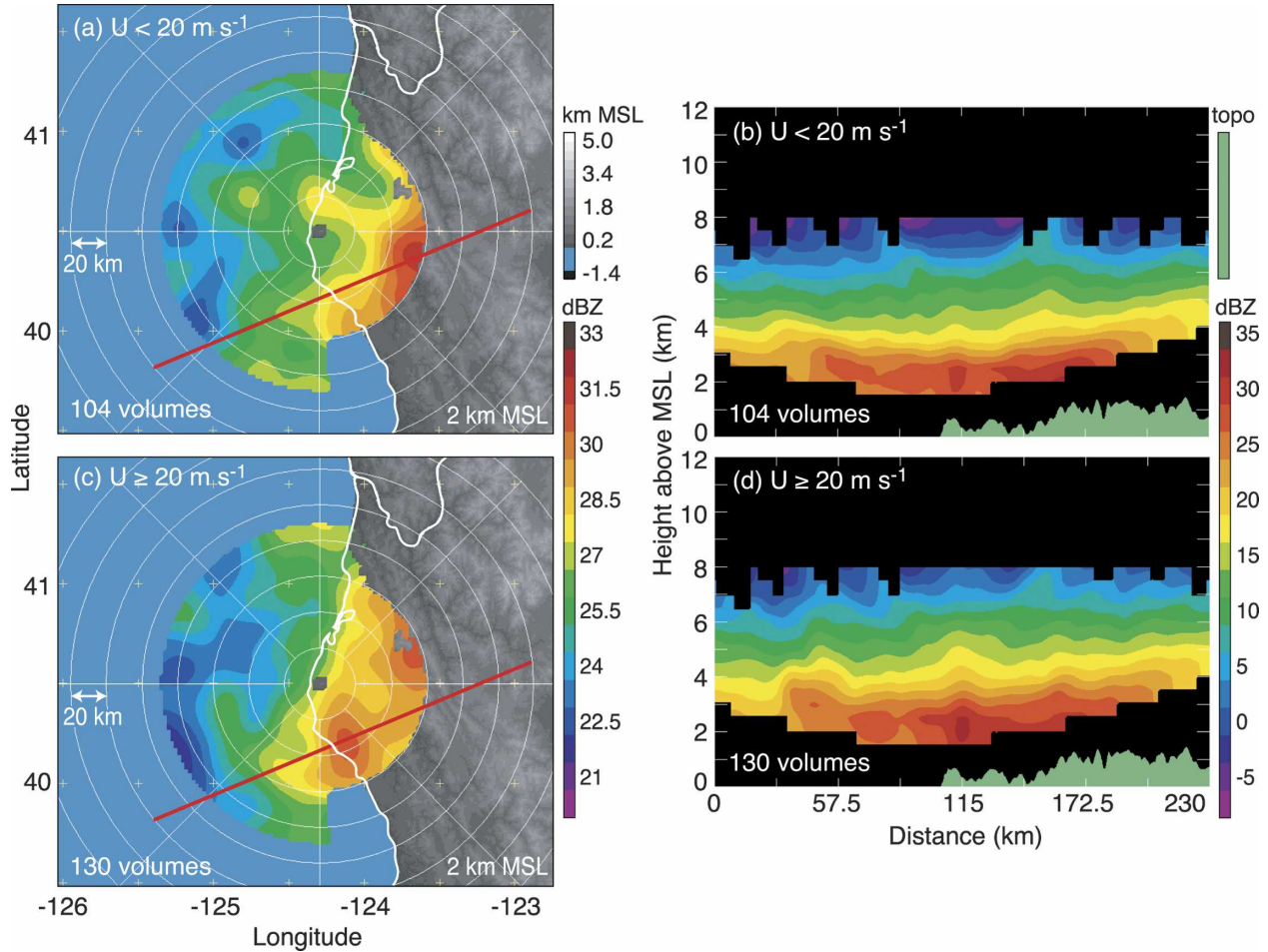
FIG. 13. Of those volumes whose 900–800-hPa wind direction was west-southwesterly (between 225° and 270° azimuth) and the 0°C level was at least 2.5 km MSL, this analysis depicts the mean reflectivity at 2-km altitude when the layer-averaged 900–800-hPa wind speed was (a) <20 and (c) ≥20 m s^{-1}. (b) and (d) Vertical cross-section plots from west-southwest to east-northeast along the red segments (a) and (c), respectively, with the underlying terrain shaded green. Range ring spacing is 20 km, with azimuth lines drawn every 45°.

a shallow cold pool offshore is a typical feature encountered by landfalling storms in this region. But, again, we have no way to verify this hypothesis with the present dataset. The upward protrusion of echo at the leading edge of the zone of offshore enhanced echo could have been exaggerated by brightband contamination or by other range-dependent interpolation effects. However the abrupt nature of the upward protrusion suggests that it is a real feature.

The strong local reflectivity enhancement at the first large peak of terrain (King Range) seen in Figs. 13b and 13d (similar to the cross sections in Figs. 6d, 9d, and 10d) and the associated upward bulge of reflectivity contours over this first peak are consistent with the behavior of precipitation enhancement by an unblocked upslope flow (HJM; Medina and Houze 2003). A secondary maximum of reflectivity occurred at the

second major rise of terrain (at ~160 km on the horizontal scale of Figs. 13b and 13d), probably also as a result of the rise of the unblocked flow over the terrain. The maxima of reflectivity seen in the cross sections to be associated with the first and second major peaks of terrain were actually slightly offset in the downwind directions. This behavior is consistent with the results of Sinclair et al. (1997), who concluded that heavier precipitation amounts occurred immediately downwind when the cross-barrier flow was stronger.

b. Analysis V: Stability and humidity

Figure 14 divides the west-southwesterly flow events with the 0°C level ≥2.5 km MSL into the categories of neutral to slightly unstable and slightly stable (defined in section 3). In sections 3 and 6b, we noted that the stable cases had higher upstream relative humidity in
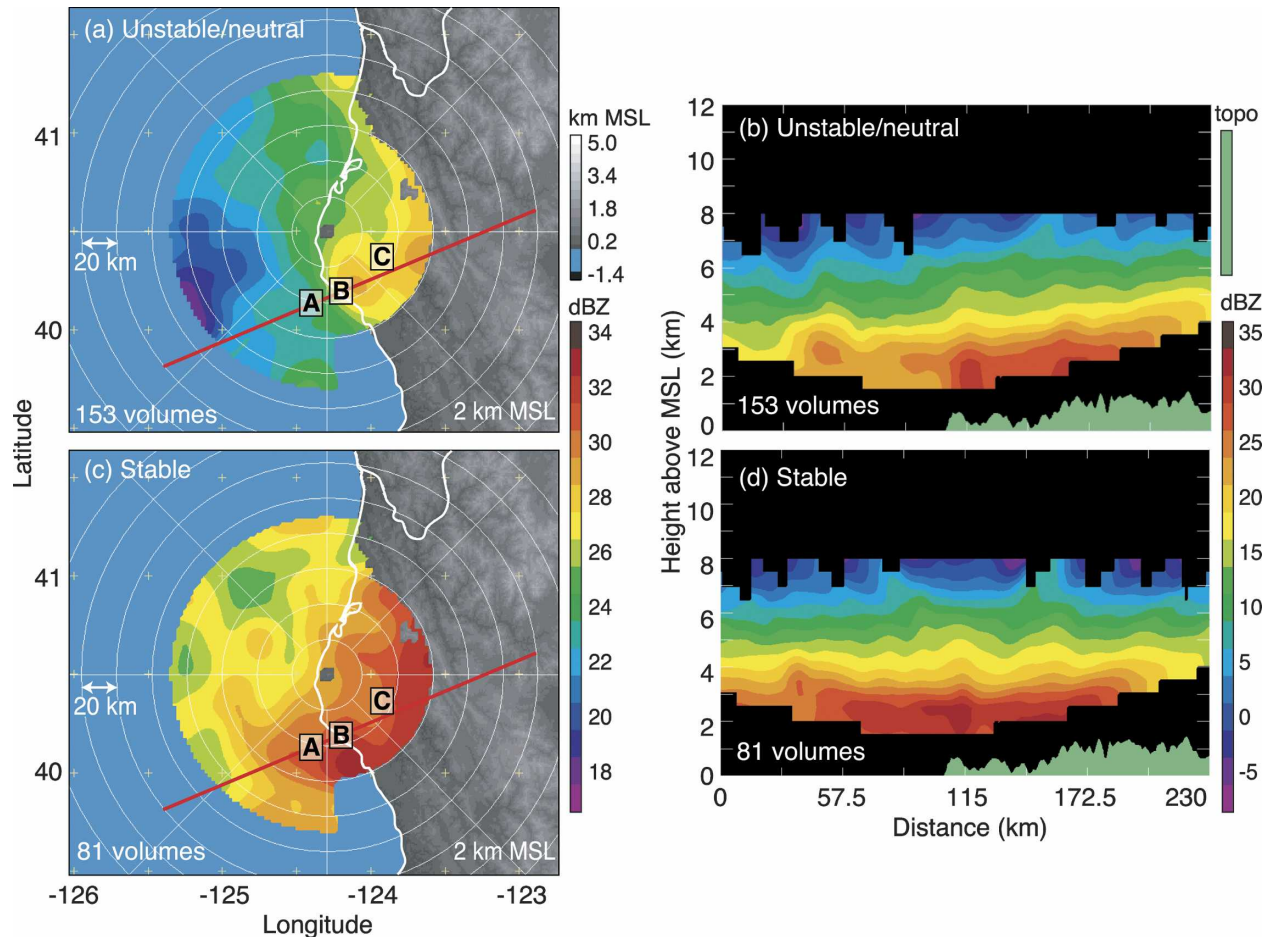
FIG. 14. As in Fig. 13, except when the layer-averaged 900–800-hPa moist Brunt–Väisälä frequency was (a) imaginary or zero and (c) greater than zero. (b) and (d) Vertical cross sections respective to (a) and (c). Bins A–C were used to create the histograms in Fig. 16.

midlevels, indicating that this subset of storms tended to have better-developed midlevel cloud layers (i.e., higher condensed water contents in the terrain-enhanced cloud areas). We also noted that the subset of stable cases had somewhat lower wind speeds above the 1-km level than did the unstable/neutral subset. Because of these synoptic differences in humidity and large-scale wind, differences between the unstable/neutral versus the stable subsets cannot be attributed solely to stability stratification.

Comparison of Figs. 14a and 14c shows that the reflectivity was stronger everywhere when absolute stability prevailed. This overall greater precipitation intensity likely reflects the generally more humid conditions in midlevels in the stable cases; that is, for synoptic reasons the stable cases had better-developed cloud layers than the unstable cases before they encountered the coastal orography. Figure 10 demonstrates the powerful influence of the higher humidity, and Fig. 5c shows that stable cases were more humid in midlevels.

In spite of the difference in overall intensity, both the more stable, more humid cases and the less stable, less humid cases were characterized by a deep broad region of stratiform echo across the entire zone of the cross sections in Figs. 14b and 14d. The offshore precipitation between the initial reflectivity core offshore and the first peak of terrain, and between the first and second peaks of terrain, exhibited a bright band under both unstable/neutral (Fig. 14b) and stable (Fig. 14d) conditions. Echo perturbations associated with the leading edge of the hypothesized offshore cold pool and the first and second major rises of terrain were embedded within the general overall continuous enhanced stratiform precipitation, as seen in previous cross sections.

In addition to exhibiting overall greater intensity, likely related to the higher humidity, the stable cases also exhibit some characteristics that appear to be related strictly to the stability. The cross section for unstable/neutral conditions in Fig. 14b shows reflectivity contours generally sloping upward over the terrain,
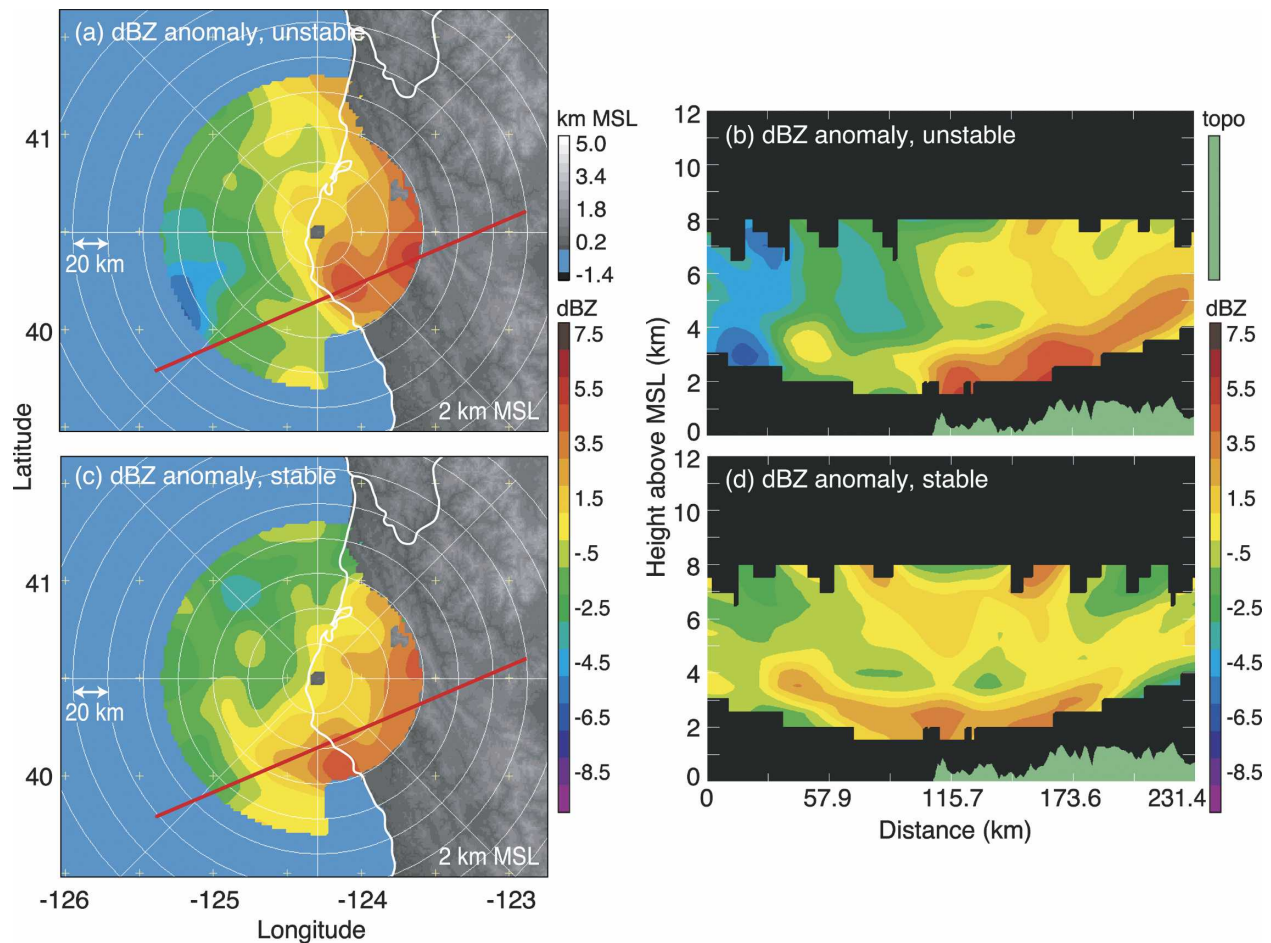
FIG. 15. As in Fig. 14, except showing the reflectivity anomaly from the horizontal mean when the 900–800-hPa moist Brunt–Väisälä frequency during west-southwesterly events (225°–270°) was (a) imaginary or zero and (c) greater than zero. (b) and (d) Vertical cross sections respective to (a) and (c). Range ring spacing is 20 km with azimuth lines drawn every 45°.

similar to cross sections in Figs. 6, 9, 10, and 13. This upward slope of contours is in concert with the broadscale upward slope of the terrain and indicates that the unstable/neutral air rose easily—that is, unblocked—over the terrain. The cross section in Fig. 14d differs noticeably from Fig. 14b in that the echo contours remain more horizontal over the terrain, thus indicating that the general upslope enhancement over the inland terrain was less than in the stable cases. Since the overall greater intensity of echo in the stable case was likely related to greater average humidity in those cases, we attempted to isolate the effect of stability by deriving the echo anomaly field by removing the mean echo pattern from Fig. 14. The results are in Fig. 15. Comparing Figs. 15b and 15d, we see that the unstable/neutral events had less offshore enhancement and greater upward sloping enhancement of echo over the inland terrain. We further note that the stable cases had a much more prominent pattern of offshore enhanced

precipitation anomaly, exhibiting a bright band and an upward echo protrusion at its leading edge.

Further insight is achieved by subdividing the reflectivity data contained within regions A, B, and C at the 1.5-km-MSL level (0.5 km lower in altitude than shown) in Fig. 14. Figure 16 displays histograms of the relative frequency of occurrence of different reflectivity values in each bin. Comparing the upstream oceanic data point A with the downstream overland points B and C, we see that under unstable/neutral conditions (Fig. 16a) the reflectivity distributions generally slowly dropped off toward lower values of reflectivity and remained relatively unchanged as the air moved inland. However, under stable conditions, the shape of the distribution changed as the air moved inland, from a broad fairly uniform distribution with somewhat of a peak at lower reflectivities over the ocean to a distribution that was sharply peaked at higher reflectivities (30–35 dBZ) over land. The orographic enhancement over land thus
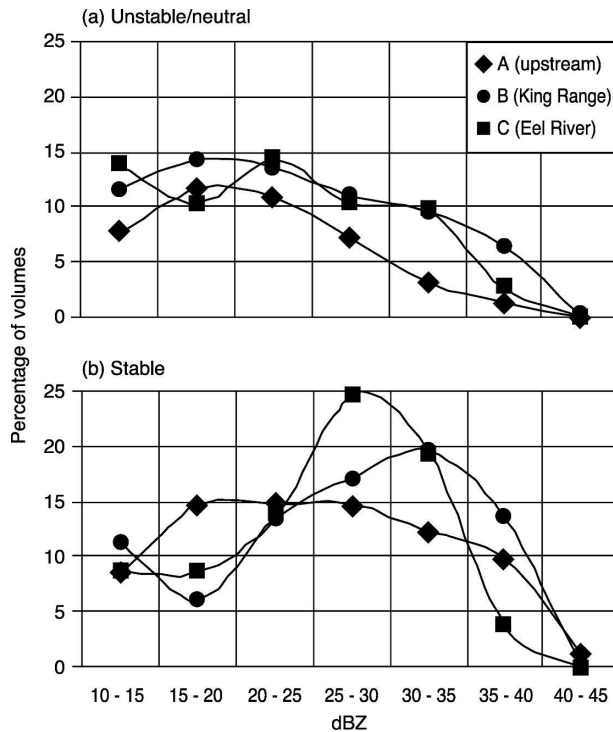
FIG. 16. Percentage of hourly radar volumes vs mean reflectivity at 1.5 km MSL within bins A–C shown in Fig. 14 when the moist Brunt–Väisälä frequency was (a) imaginary or zero and (b) greater than zero. Bin locations were chosen as follows: A is upstream from King Range, B is over King Range, and C is downwind from King Range over the Eel River.

FIG. 17. Total estimated hourly rainfall from the Eureka WSR-88D at 2-km altitude (MSL) as a function of time of day during heavy-rain events.

favored increasing the intensity as well as the frequency of precipitation over the mountains in the stable cases. This behavior over the mountains is consistent with the generally upward-sloping contours over the terrain in Fig. 14d. Recalling that the stable cases were also more humid at midlevels (Fig. 5c), we suggest that the increased intensity of the precipitation over the mountains in the subset of stable cases may be another indication that the orographic enhancement in the unblocked flow above the 1-km level results in a more robust enhancement of the frontal rainfall when the midlevel cloud layer of the frontal systems is well developed.

Another possible indication of the sensitivity of the orographic precipitation processes to stability and/or humidity appears in the diurnal variability of the echo intensity, which was similar to the diurnal patterns observed during MAP (HJM). Figure 17 depicts the average rainfall observed per hour at 2-km altitude during the 61 heavy-rain days, estimated using the reflectivity rain-rate relationship of Marshall and Palmer (1948). A maximum was observed between 3 and 9 A.M. Pacifi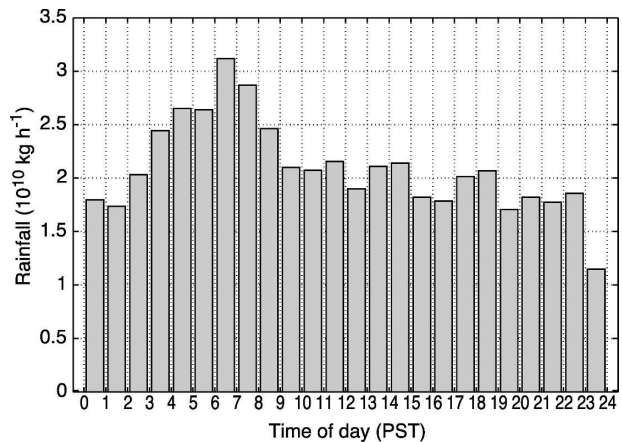c standard time (PST), with up to 60% more rainfall in the morning than other hours of the day. We suspect that higher stability combined with higher relative humidity several hours before and after dawn generates this diurnal response, which occurred 2–3 h earlier than the diurnal peak observed during MAP (HJM).

8. Conclusions

Radar reflectivity and Doppler velocity archives obtained for 61 days with major rainfall along the coast of northern California during 1 October 1995–31 March 1998 by the WSR-88D at Eureka, California, reveal the three-dimensional radar reflectivity and radial velocity fields during these events. These fields provide insight into the processes by which the interaction of the airflow with the topography modifies the precipitation processes in landfalling baroclinic storms. The major rain events occurred during southwesterly flow characterized by a low-level jet (LLJ) and a high influx of tropical moisture as described by Ralph et al. (2004). The average speed of the LLJ (observed by Doppler radar) was ~20 m s^{-1}. South of Eureka the southwesterly LLJ was perpendicular to a series of two-dimensional mountain ridges. Orographic enhancement of the precipitation occurred both over the coastal mountain ranges and upstream over the ocean. On average, the upstream enhancement occurred within about 150 km of the crest of the Coastal Range (about 60 km upstream from the coast), roughly consistent with geostrophic adjustment theory.

The flow impinging on the coastal mountains above the 1-km level was strong enough to be unblocked by the terrain. Directly over the mountains, the broad pattern of the mean reflectivity field on the scale of the

overall region of coastal mountains showed upward sloping echo contours indicative of a general upslope orographic enhancement, consistent with the unblocked flow above the 1-km level. Vertical cross sections through the climatological echo pattern of the heavy-rain events showed the precipitation to be generally stratiform in character from over the ocean to inland over the mountains. Embedded in the broadscale stratiform echo pattern over the mountains was an embedded core of maximum mean reflectivity over the first major peak of terrain encountered by the unblocked flow. This core was the strongest feature of the orographic precipitation pattern. A secondary echo core occurred over the second major peak of the coastal mountain terrain. It was similar to the core over the first peak of terrain, but not as intense. Under strong wind conditions, these cores were advected slightly downwind of the first peak. This mean embedded echo core had a maximum intensity at low levels (below the 0°C level) but extended as an upward protrusion of the reflectivity contours to high levels, to near the top of the layer of echo. The mean echo core observed at the first major peak of terrain, embedded in the broader stratiform echo structure, is similar to radar echoes observed in unblocked flows over the European Alps (HJM; Medina and Houze 2003). The precipitation growth processes contributing to the echo core over the first major peak of terrain in the Alps were determined to be coalescing below the 0°C level and riming just above the 0°C level (Medina and Houze 2003; Yuter and Houze 2003). Similar processes probably were active in the heavy-rain events over the California Coastal Range. White et al. (2003) concluded that low-level growth by coalescence was important in precipitation over the California Coastal Range. We suggest that ice processes, especially riming, are also important.

In addition to radar echoes of the type associated with unblocked flow, both on the broad scale of the entire coastal mountain region and on the scale of the local large peaks of terrain, considerable upstream echo enhancement also occurred. The offshore enhancement of radar echo could be the result of enhanced frontogenesis in the coastal zone (Yu and Smull 2000; Colle et al. 2002; Olson and Colle 2004). It is also possible that a shallow layer of cool air upstream of the coast was dammed, blocked, or pooled against the coastal mountains (Neiman et al. 2002), and a deep layer of air rapidly moving shoreward rose over this layer of cool air and thus produced upstream enhancement. Additional observational data (not available to this study) are needed to determine which of these processes is most responsible for the offshore precipitation enhancement.

The features of the orographically enhanced precipitation described above were present to some degree in all the landfalling baroclinic storms with a strong cross-barrier-directed LLJ. They indicated a strong effect of unblocked flow above 1 km crossing the coastal mountains relatively unimpeded and producing enhancement both locally and on the scale of the entire barrier. However, the degree to which each feature of the enhancement process occurred varied according to large-scale synoptic conditions. All the features were more pronounced when the 500–700-hPa flow was strong (indicating stronger baroclinic forcing), when the midlevel humidity was maximum (indicating a better-developed cloud layer in the landfalling storm), and when the low-level cross-barrier wind component was maximum (stronger LLJ). When the stability was greater, the offshore enhancement of precipitation was proportionately increased, and the general broadscale upslope enhancement inland was reduced. These results indicate a high degree of consistency in the way that orography modifies the precipitation processes in storms crossing the northern California coast.

REFERENCES

Braun, S. A., R. A. Houze Jr., and B. F. Smull, 1997: Airborne dual-Doppler observations of an intense frontal system approaching the Pacific Northwest coast. *Mon. Wea. Rev.,* **125,** 3131–3156.

Browning, K. A., 1986: Conceptual models of precipitation systems. *Wea. Forecasting,* **1,** 23–41.

——, C. Pardoe, and F. F. Hill, 1975: The nature of orographic rain at wintertime cold fronts. *Quart. J. Roy. Meteor. Soc.,* **101,** 333–352.

Buzzi, A., N. Tartaglione, and P. Malguzzi, 1998: Numerical simulations of the 1994 Piedmont Flood: Role of orography and moist processes. *Mon. Wea. Rev.,* **126,** 2369–2383.

Caracena, F., R. A. Maddox, L. R. Hoxit, and C. F. Chappell, 1979: Mesoanalysis of the Big Thompson Storm. *Mon. Wea. Rev.,* **107,** 1–17.

Colle, B. A., C. F. Mass, and B. F. Smull, 1999: An observational and numerical study of a cold front interacting with the Olympic Mountains during COAST IOP5. *Mon. Wea. Rev.,* **127,** 1310–1334.

——, B. F. Smull, and M.-J. Yang, 2002: Numerical simulations of a landfalling cold front observed during COAST: Rapid evolution and responsible mechanisms. *Mon. Wea. Rev.,* **130,** 1945–1966.

Corbet, J., C. Mueller, C. Burghart, K. Gould, and G. Granger, 1994: Zeb: Software for integration, display, and management of diverse environmental datasets. *Bull. Amer. Meteor. Soc.,* **75,** 783–792.

Crum, T. D., and R. L. Alberty, 1993: Recording, archiving, and using WSR-88D data. *Bull. Amer. Meteor. Soc.,* **74,** 645–653.

Doswell, C. A., C. Ramis, R. Romero, and S. Alonso, 1998: A diagnostic study of three heavy precipitation episodes in the western Mediterranean region. *Wea. Forecasting,* **13,** 102–124.

Doviak, R. J., and D. S. Zrnic, 1993: *Doppler Radar and Weather Observations.* 2d ed. Academic Press, 562 pp.

Doyle, J. D., 1997: The influence of mesoscale orography on a coastal jet and rainband. *Mon. Wea. Rev.,* **125,** 1465–1488.

Durran, D. R., and J. B. Klemp, 1982: On the effects of moisture on the Brunt–Väisälä frequency. *J. Atmos. Sci.,* **39,** 2152–2158.

Eilts, M. D., and S. D. Smith, 1990: Efficient dealiasing of Doppler velocities using local environmental constraints. *J. Atmos. Oceanic Technol.,* **7,** 118–128.

Elliott, R. D., and E. L. Hovind, 1964: On convection bands within Pacific Coast storms and their relation to storm structure. *J. Appl. Meteor.,* **3,** 143–154.

Grossman, R. L., and D. R. Durran, 1984: Interaction of low-level flow with the western Ghat Mountains and offshore convection in the summer monsoon. *Mon. Wea. Rev.,* **112,** 652–672.

Hobbs, P. V., R. A. Houze Jr., and T. J. Matejka, 1975: The dynamical and microphysical structure of an occluded frontal system and its modification by orography. *J. Atmos. Sci.,* **32,** 1542–1562.

——, T. J. Matejka, P. H. Herzegh, J. D. Locatelli, and R. A. Houze Jr., 1980: The mesoscale and microscale structure and organization of clouds and precipitation in midlatitude cyclones. I: A case study of a cold front. *J. Atmos. Sci.,* **37,** 568–596.

Houze, R. A., Jr., 1993: *Cloud Dynamics.* Academic Press, 573 pp.

——, and S. Medina, 2005: Turbulence as a mechanism for orographic precipitation enhancement. *J. Atmos. Sci.,* **62,** 3599–3623.

——, J. D. Locatelli, and P. V. Hobbs, 1976: Dynamics and cloud microphysics of the rainbands in an occluded frontal system. *J. Atmos. Sci.,* **33,** 1921–1936.

——, S. A. Rutledge, M. I. Biggerstaff, and B. F. Smull, 1989: Interpretation of Doppler weather radar displays in midlatitude mesoscale convective systems. *Bull. Amer. Meteor. Soc.,* **70,** 608–619.

——, C. N. James, and S. Medina, 2001: Radar observations of precipitation and airflow on the Mediterranean side of the Alps: Autumn 1998 and 1999. *Quart. J. Roy. Meteor. Soc.,* **127,** 2537–2558.

James, C. N., S. R. Brodzik, H. Edmon, R. A. Houze Jr., and S. E. Yuter, 2000: Radar data processing and visualization over complex terrain. *Wea. Forecasting,* **15,** 327–338.

Kalnay, E., and Coauthors, 1996: The NCEP/NCAR 40-Year Reanalysis Project. *Bull. Amer. Meteor. Soc.,* **77,** 437–471.

Marshall, J. S., and W. M. Palmer, 1948: The distribution of raindrops with size. *J. Meteor.,* **5,** 165–166.

Medina, S., and R. A. Houze Jr., 2003: Air motions and precipitation growth in Alpine storms. *Quart. J. Roy. Meteor. Soc.,* **129,** 345–371.

——, B. F. Smull, R. A. Houze Jr., and M. Steiner, 2005: Cross-barrier flow during orographic precipitation events: Results from MAP and IMPROVE. *J. Atmos. Sci.,* **62,** 3580–3598.

Mohr, C. G., and R. L. Vaughan, 1979: An economical procedure for Cartesian interpolation and display of reflectivity factor data in three-dimensional space. *J. Appl. Meteor.,* **18,** 661–670.

Nagle, R. E., and S. M. Serebreny, 1962: Radar precipitation echo and satellite cloud observations of a maritime cyclone. *J. Appl. Meteor.,* **1,** 279–295.

Neiman, P. J., F. M. Ralph, A. B. White, D. E. Kingsmill, and P. O. G. Persson, 2002: The statistical relationship between upslope flow and rainfall in California's coastal mountains: Observations during CALJET. *Mon. Wea. Rev.,* **130,** 1468–1492.

——, P. O. G. Persson, F. M. Ralph, D. P. Jorgensen, A. B. White, and D. E. Kingsmill, 2004: Modification of fronts and precipitation by coastal blocking during an intense landfalling winter storm in southern California: Observations during CALJET. *Mon. Wea. Rev.,* **132,** 242–273.

Olson, J. B., and B. A. Colle, 2004: Idealized three-dimensional simulations of fronts interacting with the U.S. West Coast topography. Preprints, *11th Conf. on Mountain Meteorology and the Annual Mesoscale Alpine Program,* Bartlett, NH, Amer. Meteor. Soc., CD-ROM, 4.5.

Queney, P., 1948: The problem of airflow over mountains: A summary of theoretical results. *Bull. Amer. Meteor. Soc.,* **29,** 19–26.

Ralph, F. M., and Coauthors, 1999: The California Land-Falling Jets Experiment (CALJET): Objectives and design of a coastal atmosphere–ocean observing system deployed during a strong El Niño. Preprints, *Third Symp. on Integrated Observing Systems,* Dallas, TX, Amer. Meteor. Soc., 78–81.

——, P. J. Neiman, and G. A. Wick, 2004: Satellite and CALJET aircraft observations of atmospheric rivers over the eastern North Pacific Ocean during the winter of 1997/98. *Mon. Wea. Rev.,* **132,** 1721–1745.

——, ——, and R. Rotunno, 2005: Dropsonde observations in low-level jets over the northeastern Pacific Ocean from CALJET-1998 and PACJET-2001: Mean vertical-profile and atmospheric-river characteristics. *Mon. Wea. Rev.,* **133,** 889–910.

Reed, R. J., and E. E. Recker, 1971: Structure and properties of synoptic-scale wave disturbances in the equatorial western Pacific. *J. Atmos. Sci.,* **28,** 1117–1133.

Rotunno, R., and R. Ferretti, 2001: Mechanisms of intense alpine rainfall. *J. Atmos. Sci.,* **58,** 1732–1749.

Sinclair, M. R., D. S. Wratt, R. D. Henderson, and W. R. Gray, 1997: Factors affecting the distribution and spillover of precipitation in the southern Alps of New Zealand: A case study. *J. Appl. Meteor.,* **36,** 428–442.

Smith, R. B., 1979: The influence of mountains on the atmosphere. *Advances in Geophysics,* Vol. 21, 87–230.

Sommerfield, C. K., D. E. Drake, and R. A. Wheatcroft, 2002: Shelf record of climatic changes in flood magnitude and frequency, north-coastal California. *Geology,* **30,** 395–398.

Spiegel, M. R., 1972: *Schaum's Outline of Theory and Problems of Statistics.* McGraw-Hill, 359 pp.

Westrick, K. J., C. F. Mass, and B. A. Colle, 1999: The limitations of the WSR-88D radar network for quantitative precipitation measurement over the coastal western United States. *Bull. Amer. Meteor. Soc.,* **80,** 2289–2298.

White, A. B., P. J. Neiman, F. M. Ralph, D. E. Kingsmill, and P. O. G. Persson, 2003: Coastal orographic rainfall processes observed by radar during the California Land-Falling Jets Experiment. *J. Hydrometeor.,* **4,** 264–282.

Wilks, D. S., 1995: *Statistical Methods in the Atmospheric Sciences.* Academic Press, 467 pp.

Yu, C.-K., and B. F. Smull, 2000: Airborne observations of a landfalling cold front upstream of steep coastal orography. *Mon. Wea. Rev.,* **128,** 1577–1603.

Yuter, S. E., and R. A. Houze Jr., 2003: Microphysical modes of precipitation growth determined by S-band vertically pointing radar in orographic precipitation during MAP. *Quart. J. Roy. Meteor. Soc.,* **129,** 455–476.